NANOCAT
NANOTECHNOLOGY AND CATALYSIS RESEARCH CENTRE

eISSN 2811-3756

Malaysian Catalysis
An International Journal

# MALAYSIAN CATALYSIS
## AN INTERNATIONAL JOURNAL

Volume 1, Issue 2
2021

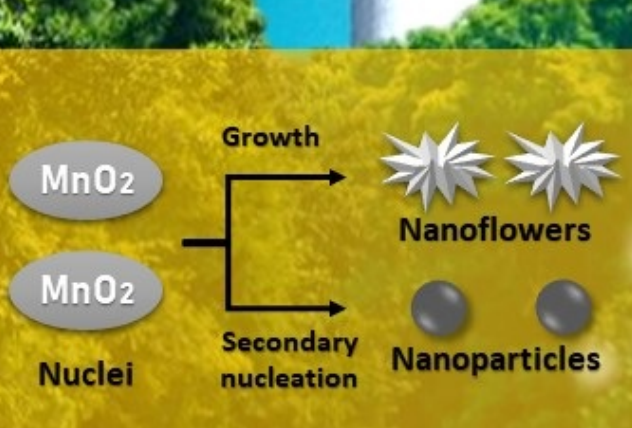


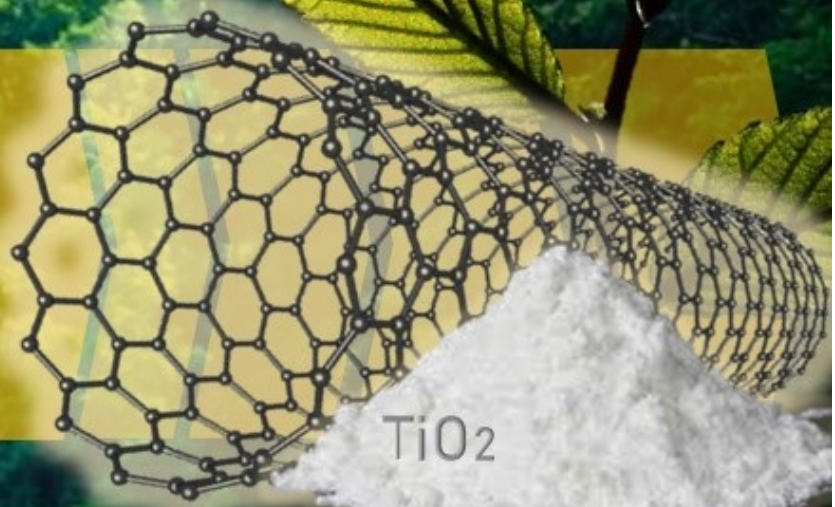

Malaysian Catalysis-An International Journal

*Malay. Catal.Int.J Vol 1, Issue 2 (2021) 01-11*

# ARTICLE TYPE

# Synthesis of $MnO_2$ Particles via One Step Localized Heating Method as Catalyst for Dye Degradation

S.L.Chiam, S. Y. Pung*[a.]

[a] School of Materials and Mineral Resources Engineering, Engineering Campus, Universiti Sains Malaysia, 14300 Nibong Tebal, Pulau Pinang, Malaysia

Received 5th Oct 2021,
Revised 3rd Dec 2021,
Accepted 6th Dec 2021

DOI: 10.22452/mcij.vol1no2.1

*Corresponding author*:
sypung@usm.my

## Abstract

This work demonstrated the synthesis of $MnO_2$ particles via a rapid one-step localized heating method. The heat was transferred directly from the wire into the precursor solution, minimizing the heat loss to the surrounding. As a result, the precursor solution was heated up rapidly and $MnO_2$ particles with different morphologies were successfully synthesized in a short duration within 10 to 15 min. These $MnO_2$ particles were used as catalysts in the degradation of Rhodamine B (RhB) organic dye. Particularly, $MnO_2$ particles synthesized at 10 min possessed outstanding catalytic activity with 99% degradation efficiency of RhB dye in 10 min of reaction time. This was significantly contributed by its 3D nanoflowers morphology, which provided more active sites for catalytic activities. The promising catalytic activity, synthesizing by a simple and affordable synthesis setup could provide an alternative in developing $MnO_2$ catalyst for organic pollutants removal.

Keywords: Manganese dioxide ($MnO_2$), nanoflowers; catalyst; dye degradation; rapid synthesis

## 1.0 Introduction

$MnO_2$, which is categorized as n-type semiconductor, possesses band gap energy in the range of 1–2 eV [1]. It is one of the promising candidates in the removal of organic dye [2-4]. It possesses various redox activities due to its different oxidation states (+2, +3 and +4), low toxicity, and abundancy. These unique properties make it an attractive potential catalyst for wastewater treatment [5, 6]. In addition, $MnO_2$ particles are approximately 75% cheaper than the commonly used photocatalyst, for example $TiO_2$ particles. One kilogram of $MnO_2$ particles costs USD 600 whereas one kilogram of $TiO_2$ particles will need USD 2850 (information obtained from www.sigmaaldrich.com).

Numerous approaches have been reported in the synthesis of $MnO_2$ particles such as hydrothermal [7], sol-gel [1], wet chemical [8], precipitation [9], microwave [10], ice-templating [11], reflux [12] and mechanochemical process [13]. Among these methods, hydrothermal, sol-gel, and precipitation are frequently reported in the synthesis of $MnO_2$ particles. Their synthesis processes are simple, easy to repeat, and the size and morphology can be easily tailored by changing the reaction's parameters. However, attributed to their setups, these methods usually require relatively lengthy synthesis time (>8 h) and high usage of electrical energy (>200 W h) [14]. These methods are considered inefficient in terms of energy and time as the heat generated by the heating coils is transferred externally from the reactor system to the precursor solution. Most of the heat is lost during this process. This became the main drawback for practical application which require mass production at a low cost of synthesis

A rapid synthesis of $MnO_2$ particles via the localized heating (LH) method is reported in this paper. Once the electric current was passed through the wire, the heat was generated and was transferred directly to the target solution. This approach minimizes the heat lost to the surrounding. With this, high heating rate was attained and $MnO_2$ particles were successfully produced in a short duration (10 min) with low usage of electrical energy (≈ 40W h). The $MnO_2$ particles demonstrated promising catalytic activity attributed to their 3D nanoflowers morphology that offered a large surface area for dye removal.

## 2.0 Materials and Methods

### 2.1 Synthesis of $MnO_2$ particles

The precursor solution was prepared using a 2:3 molar ratio of $KMnO_4$ (0.70 g) and $MnSO_4$ (1.125 g) which dissolved in distilled water (80 ml). A benchtop power regulator was used to pass the electrical current to the wire that submerged in the precursor solution under constant stirring. The temperatures of the wire and the precursor solution were monitored by thermocouples. The particles collected were then washed with ethanol and distilled water before drying at room temperature. The effect of heating duration was studied.

### 2.2 Materials Characterization

Field emission scanning electron microscopy (FESEM, Zeiss Supra 35 VP) and Tecnai G2 F20 X-Twin transmission electron microscope (TEM) were used to study the surface morphologies of the

particles. X-ray diffraction (XRD) analysis using a D8 Advance (Bruker, Karlsruhe, Germany) automated X-ray diffractometer system was used to identify the crystal phases of the particles. UV-Visible spectroscopy (Varian Cary 50) was used to study the catalytic activity of the particles.

### 2.3 Catalytic removal of RhB dye

$MnO_2$ particles (0.025 g) were added into the beaker filled with RhB solution (250 ml, 2.5 mg/L). At given time intervals, the mixed solution (2.5 ml) was collected. The absorbance of solution collected at different time intervals was measured by UV-Vis spectrometer. The degradation efficiency was calculated from the absorption of RhB at 554 nm using **Eq. 1.**

$$\text{Removal efficiency (\%)} = \frac{A_o - A_t}{A_o} \times 100 \qquad (1)$$

where $A_o$ and $A_t$ is the absorbance of RhB aqueous solution at t=0 min and after t min of reaction respectively. The kinetics of the degradation process were calculated based on the pseudo-first-order kinetic model using **Eq. 2**.

$$\ln(A_0/A_t) = kt \qquad (2)$$

where $A_o$ and $A_t$ are the concentration of RhB at t=0 min and after t min of reaction respectively.

### 3.0 Results and discussion

Figure 1 illustrates the XRD profiles of the particles synthesized at a heating duration of 10 and 15 min. The XRD profiles show a similar diffraction pattern where there are five broad diffraction peaks detected at 11.59 °, 23.76 °, 37.23 °, 42.08 °and 66.69 ° corresponding to (110), (220), (211), (031) and (002) crystal planes of $MnO_2$ (JCPDS 44-141). Besides, both profiles display broad diffraction peaks. This suggests that the $MnO_2$ particles possessed amorphous structures.

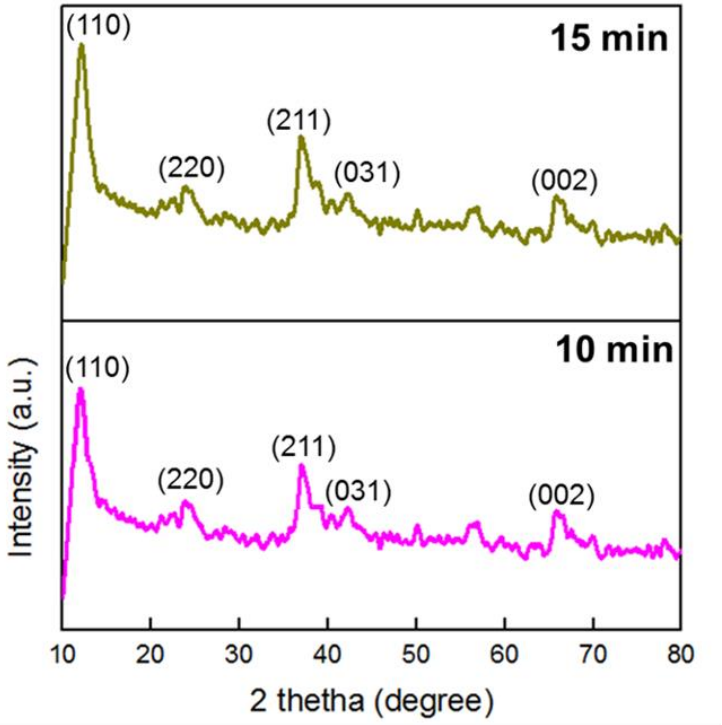


**Figure 1:** XRD profiles of $MnO_2$ particles synthesized at different heating duration.

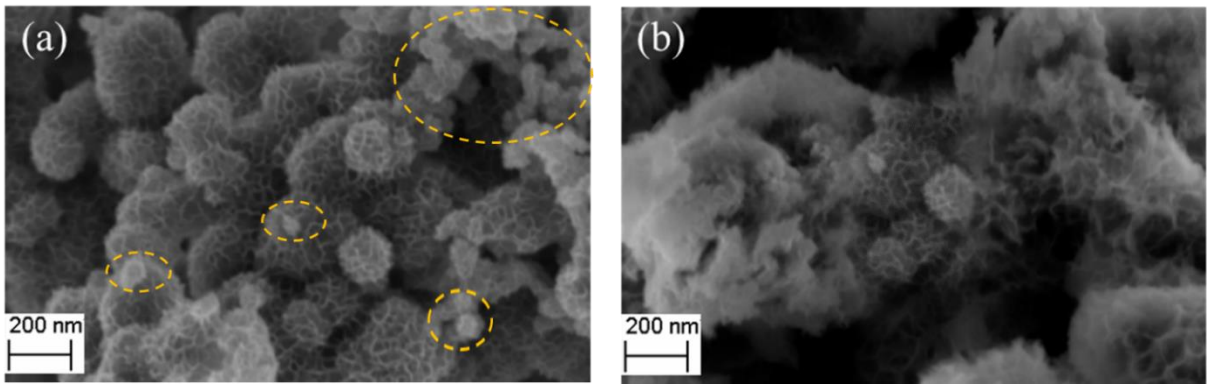


**Figure 2:** FESEM images of $MnO_2$ particles synthesized at heating duration of (a) 10min (circled area represent small particles) and (d) 15 min at a magnification of 30K .

Figures 2a and b illustrate the morphologies of $MnO_2$ particles synthesized at a heating duration of 10 and 15 min. The $MnO_2$ particles possessed different morphologies in general. At 10 min, hierarchical flower-like structures was formed. These flower-like particles were made up of assemblies of thin intersected nanosheets. Besides, tiny particles were found deposited on the surface of $MnO_2$ nanoflowers as highlighted in the yellow circle. By increasing the heating duration to 15 min, agglomerated structures were observed over the surface of $MnO_2$ particles.

The growth mechanism of $MnO_2$ particles using the LH method is proposed in Figure 3. As illustrated in Figure 3a, the temperature of wire and solution was 28 °C at t=0 min. Since there was no current supply, no heat was generated from the wire. Therefore, no $MnO_2$ particles were synthesized. After switching for 10 min, the temperature of the wire reached 85 °C while the temperature of the adjacent precursor solution was 80 °C. This observation suggests that heat transferred rapidly into the precursor solution. This is explainable as LH method allowed the transfer of heat constantly and directly into the precursor solution. This offered more efficient energy transfer and thus high heating rate. The temperature of the precursor solution was sufficient to initiate the redox reaction between $KMnO_4$ and $MnSO_4$. According to Classic Nucleation Theory (CNT), under high heating rate, nucleation reaction will be triggered within a short time. This in turn would offer a higher concentration of nucleus. The MnO2 nuclei formed in the precursor solution would self-assembly and grow into crumpled and intersected nanoflowers as shown in Figure 2a. Besides, secondary nucleation could also occur under rapid heating rate conditions [15, 16]. Small particles were formed and deposited on the surface of MnO2 nanosheets.

Most of the precursor in the solution was depleted when the heating duration was prolonged to 15 min. Subsequently, a slower nucleation rate was observed. Meanwhile, Ostwald ripening occurred in the solution that was heated under uniform temperature. This phenomenon was frequently seen in the solid-solutions medium where the small crystals redeposit onto a larger crystal over time as observed in Figure 2b.

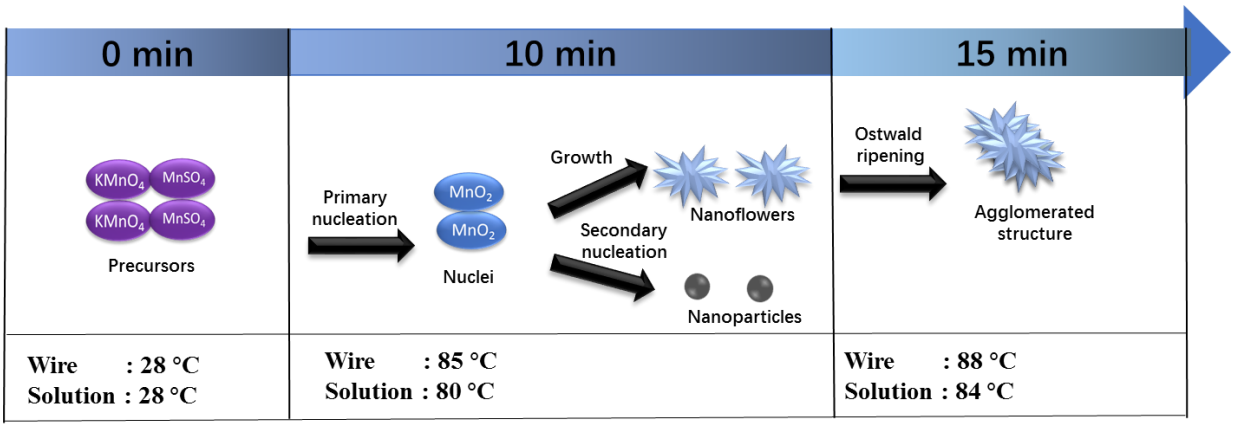


**Figure 3**: A schematic diagram illustrates the morphology evolution of $MnO_2$ particles nanoflowers with heating durations.

The catalytic activities of $MnO_2$ particles were investigated by assessing their removal efficiency towards the RhB dye. The UV–Vis profiles of RhB dye with $MnO_2$ particles synthesized at 10 min and 15 min are shown in Figure 4. Both the characteristic peaks of RhB at the wavelength of 554 nm decreased with time. The distinct peaks of $MnO_2$ particles synthesized at 10 min reduced faster than those synthesized at 15 min. The relative intensity of the absorption peaks for $MnO_2$ synthesized at 10 min vanished entirely after 20 min of reaction time.

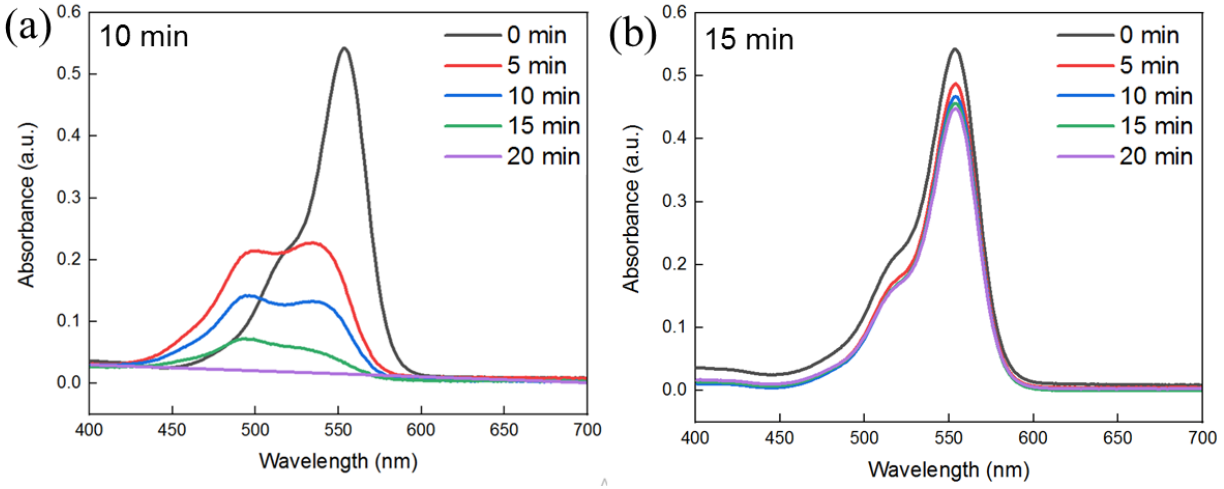


**Figure 4:** UV–Vis absorption profile of RhB as a function of reaction time using $MnO_2$ particles synthesized at (a) 10 min and (b) 15 min.

The characteristic absorbance peak of RhB is 554 nm. The decrease of absorbance at 554 nm indicates that the reduction of RhB concentration in solution. The removal of RhB from the solution could be via degradation, adsorption or a combination of both mechanisms. $MnO_2$ particles synthesized at 10 min displayed a blue shift in the wavelength. The wavelength was shifted from 554 nm to 449 nm suggests the degradation of RhB molecules via the formation of nitrogen-centered radicals, which underwent a two-step reaction of N-deethylation followed by the destruction of the backbones. Thus, this is solid evidence that the removal of RhB by $MnO_2$ particles synthesized at 10 min was through the degradation process. On the contrary, no apparent band shift was observed when using $MnO_2$ particles synthesized at 15 min. As both $MnO_2$ particles were synthesized using the same process, except synthesis duration, thus it is strongly believed that the removal of RhB by $MnO_2$ particles synthesized at 15 min was also through the degradation process. Nevertheless, the degradation process was much slower than $MnO_2$ synthesized at 10 min. Thus, the shifting of absorbance peak was not observed during the photocatalytic test.

A plot of removal efficiency of RhB with time is demonstrated in Figure 5a using Eq. 1 to evaluate their catalytic activities quantitatively. The self-degradation of RhB is negligible as it is less than 1.0%. The degradation efficiency of $MnO_2$ particles synthesized at 10 min and 15 min were 99 % and 17 % respectively. The kinetics of the degradation process of RhB by $MnO_2$ particles were explored. The linear fittings in Figure 5b indicated that the degradation of RhB by these $MnO_2$ particles followed the pseudo-first order kinetic model. The reaction rate constants of $MnO_2$ particles synthesized at 10 min and15 min were 0.162 and 0.010 min− 1 respectively. The $MnO_2$ particles synthesized at 10 min possessed the highest removal efficiency. Its efficiency is approximately 6 folds more elevated than $MnO_2$ synthesized at 15 min.

Next, the repeatability test on the catalytic performances of $MnO_2$ particles synthesized at 10 min in subsequent five cycles are shown in (Figure 5c). $MnO_2$ particles can maintain their catalytic efficiency up to 70% after reusing for five cycles. It can be concluded that the outstanding catalytic activity of $MnO_2$ particles synthesized at 10 min was significantly contributed by its hierarchical flower-like morphology that provided more active sites for catalytic activities to occur. According to a previously reported study, 3D nanoflowers in a minute structure provided a high surface area to volume ratio, which increased the chance of adsorption of dye molecules, providing a high rate of reaction and hence high removal rate on RhB dye [17, 18].

Lastly, the catalytic performance of $MnO_2$ particles synthesized at 10 min was compared with other $MnO_2$ based catalysts reported recently. The synthesized $MnO_2$ catalyst outperformed other reported catalysts. Besides, the synthesis duration is the shortest, proving its feasibility for practical application.

**Table 1:** Catalytic activity of $MnO_2$ based catalyst in RhB dye degradation reported in the literature

| *Catalyst* | Synthesis method | Synthesis duration (hr) | Target pollutant/ concentration (mg/L) | Catalyst concentration (g/L) | Reaction time (min) | Removal efficiency (%) | Activator | Ref |
|---|---|---|---|---|---|---|---|---|
| *$MnO_2/SiO_2$ core-shell* | Mixing & calcination | 6 | RhB / 5.0 | 0.5 | 90 | 84.9 | Acid | [19] |
| *Amorphous $MnO_2$* | Mechanochemical | 5 | RhB / 9.5 | 0.16 | 30 | 99 | UV light & acid | [20] |
| *$MnO_2$/ carbon aerogel* | Hydrothermal | 2 | RhB / - | 1.5 | 80 | 99.5 | $H_2O_2$ | [21] |
| *$MnO_2/Mn_3O_4/Fe_3O_4$* | Hydrothermal | 6 | RhB / 10.0 | 0.015 | 130 | 94.5 | Visible light | [22] |
| *$\alpha MnO_2$/ Palygonskite* | Hydrothermal | 8 | RhB / 20.0 | 0.1 | 180 | 100 | PMS & Acid | [2] |
| *$MnO_2$ particles* | Localized heating | 0.16 | RhB / 2.5 | 0.1 | 20 | 99 | Acid | **This work** |

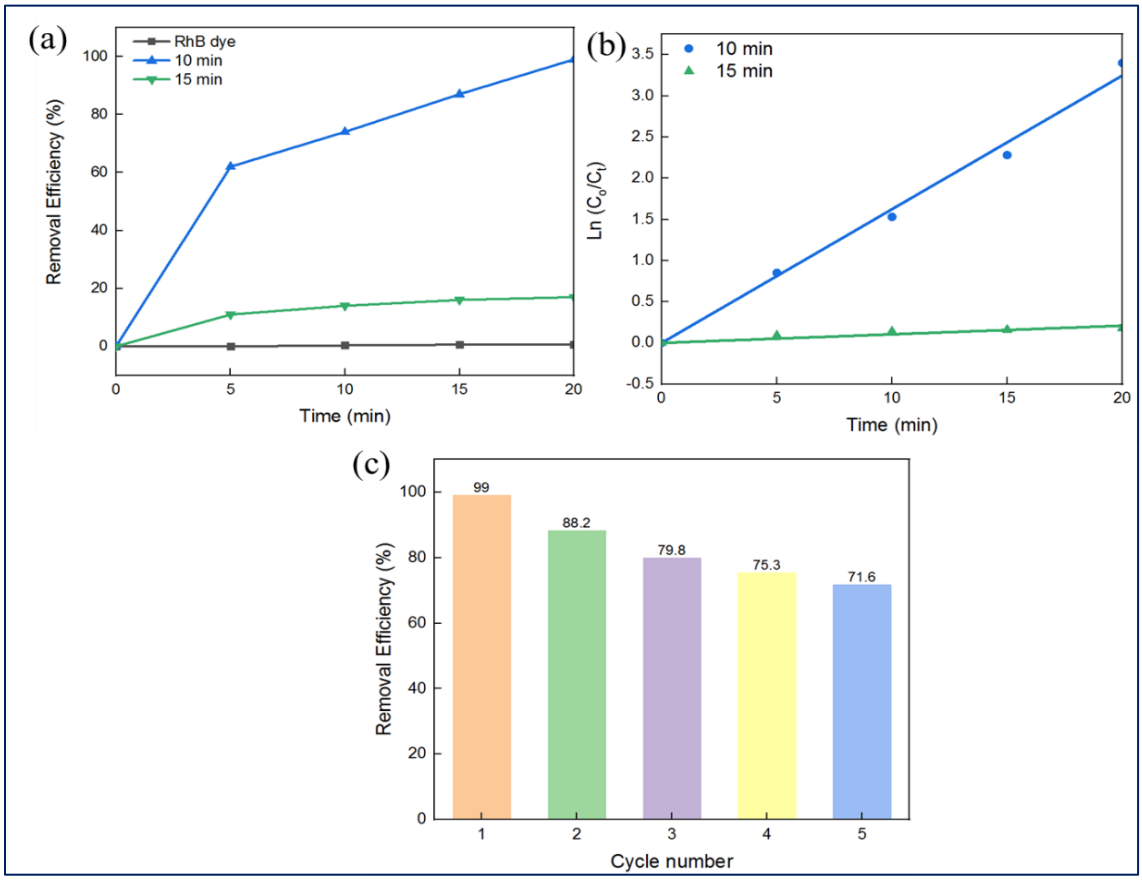


**Figure 5:** (a) Removal efficiency, (b) rate of removal and (c) repeatability test (10 min) of $MnO_2$ particles.

## Conclusion

In summary, the synthesis of $MnO_2$ particles could be achieved in a short duration of 10 min using the one-step localized heating method. The underlying mechanism for the formation of $MnO_2$ particles followed to Classical Nucleation Theory. It involved nucleation of precursors, followed by the growth of flower-like $MnO_2$ particles. Besides, tiny particles due to secondary nucleation were deposited on the surface of $MnO_2$ particles. Meanwhile, prolonging the heating duration led to Ostwald ripening, resulting in the formation of agglomerated structure. The practical application of these $MnO_2$ particles was tested by measuring their catalytic activity on the degradation of RhB organic dye. The $MnO_2$ particles synthesized at 10 min possessed the best catalytic activity. Besides, they could re-use at least cycles with efficacy maintained up to 70 %. The outstanding catalytic activity of these $MnO_2$ could be attributed to their unique 3D nanoflowers morphology, which provided a large surface area to volume ratio for a catalytic activity to occur. This work presents a simple, facile, and efficient synthesis route for $MnO_2$ particles.

## Acknowledgments

The authors acknowledge the research funding (RUI USM 1001/PBAHAN/ 8014095) from Universiti Sains Malaysia.

## Competing interests

The authors declare no competing of interest.

## References

1. Y.L. Chan, S.Y. Pung, S. Sreekantan, F.Y. Yeoh, Photocatalytic activity of β-$MnO_2$ nanotubes grown on PET fiber under visible light irradiation. *J. Exp. Nanosci.* **2016**, 11(8), 603-618.
2. C. Huang, Y. Wang, M. Gong, W. Wang, Y. Mu, Z.H. Hu, α-MnO2/Palygorskite composite as an effective catalyst for heterogeneous activation of peroxymonosulfate (PMS) for the degradation of Rhodamine B. *Sep. Purif. Technol,* **2020,** 230, 115877.
3. X. Bi, Y. Huang, X. Liu, N. Yao, P. Zhao, X. Meng, D. Astruc, Oxidative degradation of aqueous organic contaminants over shape-tunable MnO2 nanomaterials via peroxymonosulfate activation. *Sep. Purif. Technol.,* **2021,** 119141.
4. M. Cao, Z. Zhuang, Y. Liu, Z. Zhang, J. Xuan, Q. Zhang, W. Wang, Peptide-mediated green synthesis of the MnO2@ ZIF-8 core-shell nanoparticles for efficient removal of pollutant dyes from wastewater via a synergistic process. *J. Colloid Interface Sci,* **2021,** *In-press*

5. C. Fang, H. Gujarati, F. Osinaga, V. Hsia, M.A. Cheney, M.K. Kharel, Optimization of the catalytic activity of manganese dioxide (MnO2) nanoparticles for degradation of environmental pollutants. *Res. Chem. Intermed*, **2021**, 1-18
6. R. Qu, X. Li, Y. Wei, L. Feng, A bifunctional β-MnO2 mesh for expeditious and ambient degradation of dyes inactivating peroxymonosulfate (PMS) simultaneous oil removal from water. J. Colloid Interface Sci., 579, **2020**, 412-424
7. L. Xiao, W. Sun, X. Zhou, Z. Cai, F. Hu, Facile synthesis of mesoporous $MnO_2$ nanosheet and micro flower with efficient photocatalytic activities for organic dyes. *Vacuum*, **2018,** 156, 291-297.
8. P. Xia, B. Zhu, B. Cheng, J. Yu, J. Xu, 2D/2D g-$C_3N_4$/$MnO_2$ nanocomposite as a direct Z-scheme photocatalyst for enhanced photocatalytic activity. *ACS Sustain. Chem. Eng.* **2018**. 6(1), 965-973.
9. J. Chen, Z. Huang, H. Meng, L. Zhang, D. Ji, J. Liu, Z. Li, A facile fluorescence lateral flow biosensor for glutathione detection based on quantum dots-$MnO_2$ nanocomposites. *Sens. Actuators, B: Chem.* **2018,** 260, 770-777.
10. Z. Ai, L. Zhang, F. Kong, H. Liu, W. Xing, J. Qiu, J. Microwave-assisted green synthesis of $MnO_2$ nanoplates with environmental catalytic activity. *Mater. Chem. Phys.*, **2008**, 111(1), 162-167.
11. H. Sun, Y. Shang, K. Xu, Y. Tang, J. Li, Z. Liu, $MnO_2$ aerogels for highly efficient oxidative degradation of Rhodamine B. *Rsc Adv.* **2017**, 7(48), 30283-30288.
12. H.J. Cui, H. Z. Huang, B. Yuan, M.L. Fu, Decolorization of RhB dye by manganese oxides: effect of crystal type and solution pH. *Geochem. Trans*. **2015**, 16(1), 1-8.
13. T.K. Achar, A. Bose, P. Mal, Mechanochemical synthesis of small organic molecules. *Beilstein J. Org. Chem.* **2017**, 13(1) 1907-1931.
14. E.J. Kim, D. Oh, C.S. Lee, J. Gong, J. Kim, Y.S. Chang, Manganese oxide nanorods as a robust Fenton-like catalyst at neutral pH: crystal phase-dependent behavior. *Catal. Today*., **2017**, 282, 71-76.
15. Y. Yuan, S.M. Wood, K. He, W. Yao, D. Tompsett, J. Lu, R. S. Yassar, Atomistic insights into the oriented attachment of tunnel-based oxide nanostructures. *ACS nano.*, **2016,** 10(1), 539-548.
16. W. Yao, Y. Yuan, H.A. Ardakani, Z. Huang, F. Long, C.R. Friedrich, R. S. Yassar, Energy-driven surface evolution in beta-$MnO_2$ structures. *Nano Res.*, **2018**. 11(1), 206-215.
17. M.A. Alheety, S.A. Al-Jibori, A. Karadağ, H. Akbaş, M.H. Ahmed, A novel synthesis of $MnO_2$ nanoflowers as an efficient heterogeneous catalyst for oxidative desulfurization of thiophenes. *Nano-Struc. Nano-Objects*., **2019. 20**, 100392.
18. R. Yuan, Z. Jiang, Z. Wang, S. Gao, Z. Liu, M. Li, G. Boczkaj, Hierarchical $MnO_2$ nanoflowers blooming on 3D nickel foam: A novel micro-macro catalyst for peroxymonosulfate activation. *J. Colloid Interface Sci.* **2020**. 571, 142-154.
19. W. Gong, X. Meng, X. Tang, P. Ji, Core-shell MnO2-SiO2 nanorods for catalyzing the removal of dyes from water. *Catalysts*, 7(1), **2017,** 19

20. A. Gagrani, J. Zhou, T. Tsuzuki, Solvent free mechanochemical synthesis of $MnO_2$ for the efficient degradation of Rhodamine-B. *Ceram.* 44(5), **2018,** 4694-4698

21. H. Wan, H. Ge, L. Zhang, T. Duan, CS@ $MnO_2$ core-shell nanospheres with enhanced visible-light photocatalytic degradation. *Mater. Lett*, **2019,** 237, 290-293

22. M. Ma, Y. Yang, Y. Chen, F. Wu, W. Li, P. Lyu, W. Huang, Synthesis of hollow flower-like $Fe_3O_4/MnO_2/Mn_3O_4$ magnetically separable microspheres with valence heterostructure for dye degradation. *Catalysts*, **2019**, 9(7), 589

Malaysian Catalysis-An International Journal

*Malay. Catal.Int. J Vol 1, Issue 2(2021) 12-30*

**REVIEW ARTICLE**

# A systematic literature review on the effects of synthesis conditions on the physicochemical properties of activated carbons and their performance in methylene blue adsorption

K. Z. Abu Bakar [a], R. R. Nasaruddin[a,*], N. S. Engliman[a], N. Ismail[b]

a Department of Biotechnology Engineering, Kuliyyah of Engineering, International Islamic University Malaysia, 53100 Jalan Gombak, Kuala Lumpur.

b Faculty of Chemical & Process Engineering Technology, Universiti Malaysia Pahang, Lebuhraya Tun Razak, 26300 Gambang, Kuantan, Pahang

Received 03rd Dec 2021,
Revised 28th Dec 2021,
Accepted 28th Dec 2021

DOI: 10.22452/mcij.vol1no2.2

**Corresponding author*:
riccanasaruddin@iium.edu.my or
riccarahman16@gmail.com

## Abstract

This systematic literature review (SLR) describes the trend of study in activated carbons (ACs) from various biomass sources, specifically coconut shells, rice husks, and bamboo, for the adsorption of methylene blue (MB). Data acquisition and extraction from online databases were performed to review and discusses the effects of the synthesis parameters (*i.e.*, carbonization temperature and holding time) on the physicochemical properties of the synthesized ACs (*i.e.*, surface area, pore volume) and the effects of physicochemical properties to the MB adsorption. The SLR shows that the carbonization temperatures significantly affect the surface area and pore volume of ACs synthesized from coconut shells and rice husks, while ACs synthesized from bamboo were significantly influenced by the holding time. MB adsorption by ACs from all three biomasses increased with the increasing surface area and pore volume. This SLR could be a guideline to the synthesis ACs from biomass for the removal of dye in wastewater.

*Keywords: Activated Carbon*; *Coconut Shell, Rice Husk, Bamboo, Biomass Waste*; *MB Adsorption; Systematic Literature Review*

## 1.0 Introduction

Studies on the production of activated carbons (ACs) from various biomass sources have been emerging more recently due to their high potential as adsorbents for removing water pollutants like heavy metals and dyes from various industries. Despite the emergence of new carbonaceous materials such as carbon nanotube and graphene, ACs still preferable for industrial and

commercialized adsorbents due to their low cost, large surface area, and high porous structure. They are also better in performance and stability during the adsorption process [1].

On the other hand, various industries have been partly responsible for water pollution through the inappropriate discharge of their production effluents. Among all industries, the textile finishing industry caused the highest water pollution due to the discharge of dyes in their effluents. About 10 to 15% of the dyes exist in the effluents and methylene blue, MB ($C_{16}H_{18}C_lN_3S$) is the typical example [2]. The presence of dyes in water increases the water's turbidity, limiting the amount of sunlight that passes through the water for the photosynthesis process of aquatic plants. Therefore, the use of ACs synthesized from biomass sources would certainly be a favorable option to produce low-cost adsorbents for the adsorption of pollutants in the textile industry.

However, many biomass sources are being converted into ACs and the studies keep increasing. ACs synthesized from different biomass sources could have different physicochemical properties and adsorption performance. In addition, various factors affect the synthesis and performance of ACs. Different biomass sources could result in ACs with varying structures of pore and surface area distributions, reflecting the differences in adsorption capability towards MB removal. Hence, a comparative study is encouraging to show the correlations of the synthesis parameters to the physicochemical and adsorption properties of the ACs.

In this systematic literature review (SLR), we identified the gap of recent studies in online databases (i.e., ScienceDirect, Lens.org and Scopus) surrounding the potential ACs synthesized from biomass sources, which are abundantly available in Malaysia and specifically used for the dye removal application. Based on the research trend between 2015 and 2020, there is still a lack of comparative studies on the synthesis parameters, physicochemical properties, and MB adsorption of ACs from various biomass sources. Hence, this SLR was made to identify the top three biomass sources being used for its production. Then, comparative analyses were performed to compare and find the effects of the synthesis parameters on the physicochemical properties and the effects of the physicochemical properties on the adsorption properties of ACs in the removal of MB in wastewater.

## 2.0 Materials and Methods

### *2.1. Identification of research trend and biomass sources selection*

In this study, two types of searches were performed, requiring multiple databases to be used: patent search and scholarly works search. Both were necessary to produce a thorough analysis of the research trend in ACs in Malaysia. The selection was made based on the number of existing patents and scholarly works on the ACs. The patent search was performed using the Lens.org database. The key features of the database that allow for a better trend analysis, such as mapping keywords by countries, were also applied for this study. Meanwhile, ScienceDirect and Scopus databases were selected for the scholarly works search due to their extensive databases of reliable literature and refinement features. The selection of three biomass sources with the highest potential for ACs synthesis for dye removal application was made using the search string: ("activated carbon" AND "bamboo" AND ("methylene blue" OR "dye")) across these databases. The resulting trend in the number of published papers from recent studies (from 2015 to 2020) was analyzed for biomass selection.

### *2.2. Selection of research articles for analyses*

The identification and selection of relevant literature for the final list of papers were made by three phases of the screening process such as follows:

i. Initial phase: Advanced command search feature using the refined search string was applied.
ii. First phase: The papers were filtered based on their title and abstract.
iii. Second phase: The selection criteria were applied during full-text reading to get the final selection of literature.

After searching the list of potential papers based on the search string generated, all the documents obtained on the results page were exported as BibTex files to screen through the titles and abstracts. Only literature relevant to the current study was included for the second phase screening. The selected literature was then assessed whether they would be included or excluded based on the proposed inclusion and exclusion criteria needed to answer the research questions. The snowballing method was also applied to find additional documents relevant to the study among the resulting papers. Snowballing was done by skimming through the list of references cited in the articles, screening based on the title and abstract, and being assessed with the same inclusion and exclusion criteria. The proposed inclusion and exclusion criteria were as follows:

Inclusion Criteria:

i. Studies described ACs derived from biomass sources that are available within Malaysia.
ii. Studies described the preparation and activation methods used to produce the ACs.
iii. Studies included the adsorption or physicochemical properties of the ACs.
iv. Studies described the adsorption properties towards MB.
v. Studies must be published from 2015 to 2020.

Exclusion Criteria:

i. All systematic review, meta-analysis papers.
ii. The study paper was not written in English.
iii. Studies only described ACs derived from biomass sources that are unavailable in Malaysia.
iv. Studies described ACs derived from other non-biomass sources.
v. Studies described only ACs derived from non-abundant biomass sources in Malaysia.
vi. Studies published before 2015.

### *2.3. Data extraction & analysis*

All data extracted from selected literature were based on the formulated research questions (Table 1). The effects of synthesis conditions (carbonization temperature and holding time) on the physicochemical properties (surface area and total pore volume of ACs) derived from the selected three biomass sources were highlighted. Furthermore, the relation between the physicochemical properties and the adsorption performance of the ACs based on percentage dye removal (%) was also analyzed.

**Table 1**: Research questions formulated from PICOC strategy

| **Research Questions** | |
|---|---|
| **Main RQ** | What are the differences in dye adsorption performance of the ACs synthesized from different biomass sources for wastewater treatment application in Malaysia? |
| **Sub-RQ 1** | What are the potential ACs which can be produced from biomass sources in Malaysia for dye removal in wastewater treatment? |
| **Sub-RQ 2** | What factors contribute to the adsorption and physicochemical properties of ACs for dye removal application? |
| **Sub-RQ 3** | How do the preparation conditions affect the physicochemical properties of the synthesized ACs from different biomass sources? |

| | |
|---|---|
| **Sub-RQ 4** | How do the physicochemical properties affect the adsorption properties of ACs produced from different biomass sources? |

### *2.4. Normalization of MB removal data*

For the removal of methylene blue, it was realized that some research articles used different experimental conditions, especially on the mass of the AC, concentration of the MB and the reaction time. Therefore, the unit of the MB removal was normalized as follows:

$$\text{Normalized Removal of MB} = \frac{\text{removal of MB (\%)}}{\text{mass of AC (mg)} \times \text{concentration of MB } \left(\frac{\text{mg}}{\text{L}}\right) \times \text{contact time (h)}}$$

Therefore, the unit can be simplified as % removal of MB (mg of AC)$^{-1}$ (mg/L of MB)$^{-1}$ h$^{-1}$.

## 3. 0 Results and Discussion

Activated carbon (AC) is a versatile material composed of carbon with an amorphous solid structure with a high degree of porosity and a well-developed surface area with a wide range of functional groups on its surface [3]. ACs are widely used in many applications, but they are mainly known as adsorbents due to their highly porous structure. The most significant part of its structure is its pores, which are mainly categorized into three groups which are macropores, mesopores, and micropores [4]. With the exception of macropores that provide the least contribution, all other pores give rise to AC's preference as an adsorbent material as they increase the surface area. Their presence is the primary source of adsorption not only for water and gas but also for removing contaminants and certain chemicals from the gas and liquid substances [5]. Malaysia has contributed to many published studies on ACs synthesized from abundantly available local biomass sources. For example, based on the data collected from the Lens.org database (Fig. 1a), Malaysia has contributed up to 35.7%, 32%, and 27.9% of published studies on ACs synthesized from palm oil empty fruit bunches (EFB), palm kernel shell, and durian shell, respectively. Nonetheless, the current number of published research articles on ACs synthesized from these biomasses is still insufficient to be selected in this review which requires more extensive data on the physicochemical and adsorption properties.

As shown in Fig. 1b, the number of published papers in the databases is significantly low (< 500 papers) for ACs synthesized from palm oil EFB, palm kernel, and durian shell. In comparison to these, a higher number of papers (>1500 papers) were more focused on the coconut shell, rice husk, and bamboo, signifying the increasing interest by the science community in using these

biomasses to synthesize ACs, especially in Asian countries. Therefore, 43 research articles (were selected based on the three chosen biomass sources (coconut shell, rice husk, and bamboo) for further analysis in this review.

The initial screening resulted in a total of 190 articles. After removing 41 duplicate records, a total of 149 articles were accessed, out of which 56 articles were excluded based on their titles and abstracts. Next, 93 full-text articles were reviewed, out of which 44 studies were eligible for the qualitative analysis according to the established inclusion criteria. The 44 papers were composed of articles containing the physicochemical and adsorption properties of ACs from the three selected biomass sources with the respective distributions: coconut shell [6-22], bamboo [16, 23-34] and rice husk [35-48]. The analyses were divided into two categories: (a) synthesis conditions affecting the differences in physicochemical properties of ACs and (b) effects of physicochemical properties onto MB adsorption performance. A list of papers and tabulated information can be referred to Table S1-S3 in the electronic supplementary information.

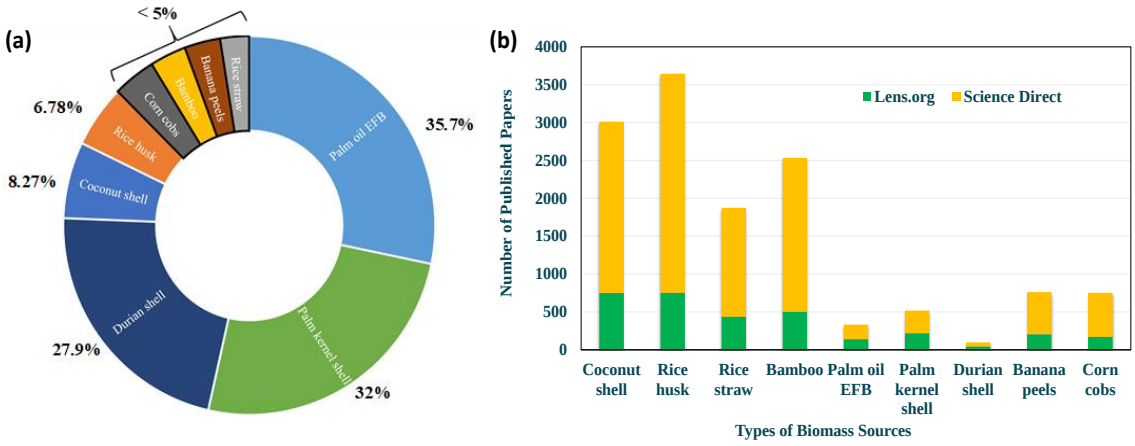


**Fig. 1:** (a) Percentage of published scholarly works on ACs synthesized from various local biomass sources contributed by research institutions within Malaysia based Lens.org database and (b) Cumulative number of published papers on ACs synthesized from different biomass sources globally from 2015 to 2020 based on Lens.org and ScienceDirect databases.

The standard method used in the synthesis of AC comprises of 2 steps: (1) carbonization and (2) activation. Depending on the precursor type, some may require the sample's additional pre-treatment process before proceeding to the two steps mentioned above. Carbonization or pyrolysis is a thermal treatment process to decompose raw materials (in this case, biomass) at higher temperatures under inert gas purge and is usually performed in a furnace. This process is the crucial

step in the production of biochar from biomass. It is necessary to improve the carbon content of the solid and remove volatile matters and tars [49]. During the carbonization process, several factors may influence the quality of the final product (AC), including the temperature as a key factor, followed by the heating rate of reaction, the amount and flow rate of the inert gas supplied, and holding time. Higher temperatures will generally result in higher amounts of volatile species released that contribute to low biochar yields. However, studies have shown that better ACs qualities can be achieved despite the low yield. Finding the right temperature is crucial. If it is too high, undesirable substances (usually tar) appear to form as deposits due to the formation of narrow pore structures of precursors during this devolatilization process [50]. Therefore, although better biochar quality can be obtained with higher temperatures, applying higher temperatures beyond the necessary values will not be feasible since it may result in a lower yield of carbon content with lower available surface area for adsorption due to the presence of tars on the AC's surface that may occupy the pores.

The carbonization process often leads to low biochar adsorption capability. As a result, an activation step is introduced to increase the biochar's surface area and pore structures, including its pore sizes. The activation process first eliminates the disorganized carbons (tarry substances that block the pores) and exposes the lignin to the activating agents to develop the microporous structures. The heat treatment at high temperature of the pores' walls would then widen up the existing meso and macropores, thus, reducing the volume of micropores.

In this step, the biochar formed earlier will be transformed into ACs and activated using various activation methods such as physical, chemical, physicochemical, or microwave-assisted activation. In some cases, the activation process takes precedence over the carbonization process; however, it depends on the biomass sources used. Physical activation consists of heat and gas (*e.g.,* steam, $CO_2$, $N_2$, or a mixture of different oxidizing gases), chemical activation by chemical agents (*e.g.,* acid, base, metal oxide, alkaline metal), physicochemical activation by heat and chemical, and microwave-assisted activation by microwave radiation [51]. The activation process depends on different parameters such as particle size, retention time, impregnation ratio, process structure, activation time, precursor properties, and chemical substances [52].

In this SLR, the comparison analysis was only done for the carbonization process's synthesis conditions: carbonization temperature and holding time. According to data extracted in Fig. 2(a-

b), Bamboo ACs have wider ranges of carbonization temperature that can be applied during the synthesis process to obtain significant surface areas and pore volumes than that of ACs from rice husk and coconut shells. On average, bamboo ACs have the surface area and pore volume between 400 to 1500 $m^2g^{-1}$ and 0.2 to 1.0 $cm^3g^{-1}$, respectively. The carbonization temperature ranged from 40 to 800$^o$C during the carbonization process. The minimum temperatures required for carbonization of bamboo into biochar are lower than the average needed for ACs, which usually kept more than 300$^o$C to achieve a high surface area (>1000 $m^2g^{-1}$) and porosity.

In addition, based on the results in Fig. 2(a), the temperature maintained at around 105$^o$C is possible for bamboo ACs to obtain a high surface area up to the range of 1456 to 2348 $m^2g^{-1}$. Even at this low temperature, a higher surface area and pore volume can be achieved by carbonizing the bamboo in an almost vacuum atmosphere (96.6% vacuum) and a longer holding time. The vacuum condition significantly reduces the pressure inside the heating chamber that can achieve a similar extent of carbonization process as when carbonized at high temperatures (700 to 800$^o$C) [23].

On the other hand, without vacuum, the surface area and the pore volume increased with the increase in carbonization temperature when performed within the range of 600 to 800$^o$C. The higher temperature resulted in mesopores and macropores' formation, thus resulting in the increased surface area of the ACs that would be useful in the adsorption for MB [27]. The presence of mesopores and macropores is encouraged for the adsorption of MB since the size of the dye particle is 1.5 nm, which would not be sufficient with the presence of only micropores (<2 nm). Therefore, larger pore sizes are necessary to allow more dye particles to diffuse into the pores and be adsorbed onto their surfaces.

Results in Fig. 2 (a-b) also show that the carbonization temperature for coconut shell ACs needed to achieve similar surface area and pore volume as bamboo ACs (500 to 1500 $m^2g^{-1}$ and 0.2 to 1.0 $cm^3g^{-1}$) was relatively limited to the range between 600 to 700$^o$C. Besides using high carbonization temperature, the high degree of the surface area of ACs can also be obtained when the ACs are made into nanofibers using the electrospinning method [6]. The advantage of using coconut shell AC nanofibers is their reusability which can maintain up to 96% at the third cycle of reusing the AC nanofibers. In another reported study, iodine-treated AC nanofibers (abbreviated as I-ACNF) resulted in the highest surface area and higher reusability than AC nanofibres without the iodine treatment (abbreviated as ACNF) and AC powder (ACP) [6]. Incorporating the iodine treatment helped retain the fiber structures. On the other hand, ACP removed a higher amount of MB relative

to the I-ACNF and ACNF. However, ACF was hard to be recycled and separated from the bulk solution due to its powder form [6].

Meanwhile, the results of the rice husk ACs in Fig. 2(a-b) show that the range of carbonization temperatures required is within the high capacity (450 to 700$^{o}$C). However, the average surface area (500 to 1000 $m^2g^{-1}$) and pore volume (0.2 to 0.6 $cm^3g^{-1}$) were slightly lower than bamboo and coconut shell ACs. Rice husk ACs resulted in a higher surface area (>1000 $m^2g^{-1}$) in the lower temperature ranges (450 to 500$^{o}$C). However, at higher temperatures beyond 500$^{o}$C, the resulting surface area significantly dropped to only 68 to 645 $m^2g^{-1}$. Higher temperatures destroyed most of the regular microporous structure during violent gasification reactions, leaving behind large holes in place [39]. Therefore, the distribution of microporous structure decreases significantly and reduces the surface area available for adsorption of the dye that would otherwise have developed at lower temperatures. When the destruction of the microporous structure has occurred, additional chemical activation that should have improved the porosity was seen not significantly to affect the already damaged structure. In addition, at temperature of 500$^{o}$C, the surface area of the sample rice husk ACs was considerably higher than the rest of the rice husk ACs (Fig. 2a). This was due to the high pore volume that reached as high as 1.8 $cm^3g^{-1}$ due to $H_3PO_4$ activation, which reacted with the silicon element naturally present in rice husk ash (rich in silica, up to 90 to 98%), resulting in the formation of phosphates that could easily be removed by washing [35].

On the other hand, graphs in Fig. 3(a-b) describe the effects of carbonization holding time on the ACs. For bamboo ACs, the holding time of 1 hour was sufficient to yield ACs with a high surface area in the range of 1000 to 2200 $m^2g^{-1}$ (Fig. 3a). When the holding time was increased from 2.5 hours to 10 hours, the surface area and pore volume could be increased from 1456 to 2348 $m^2g^{-1}$ and 0.94 to 2.3 $cm^3g^{-1}$, respectively. A significant difference was observed on the surface are of the ACs at different holding times where a wider pore distribution and significantly more pores, especially the mesopores (> 2 nm) were produced with longer holding time [23]. The higher pores and wider distribution resulted in a more porous structure, thus increasing the overall AC's surface area available for the dye adsorption.

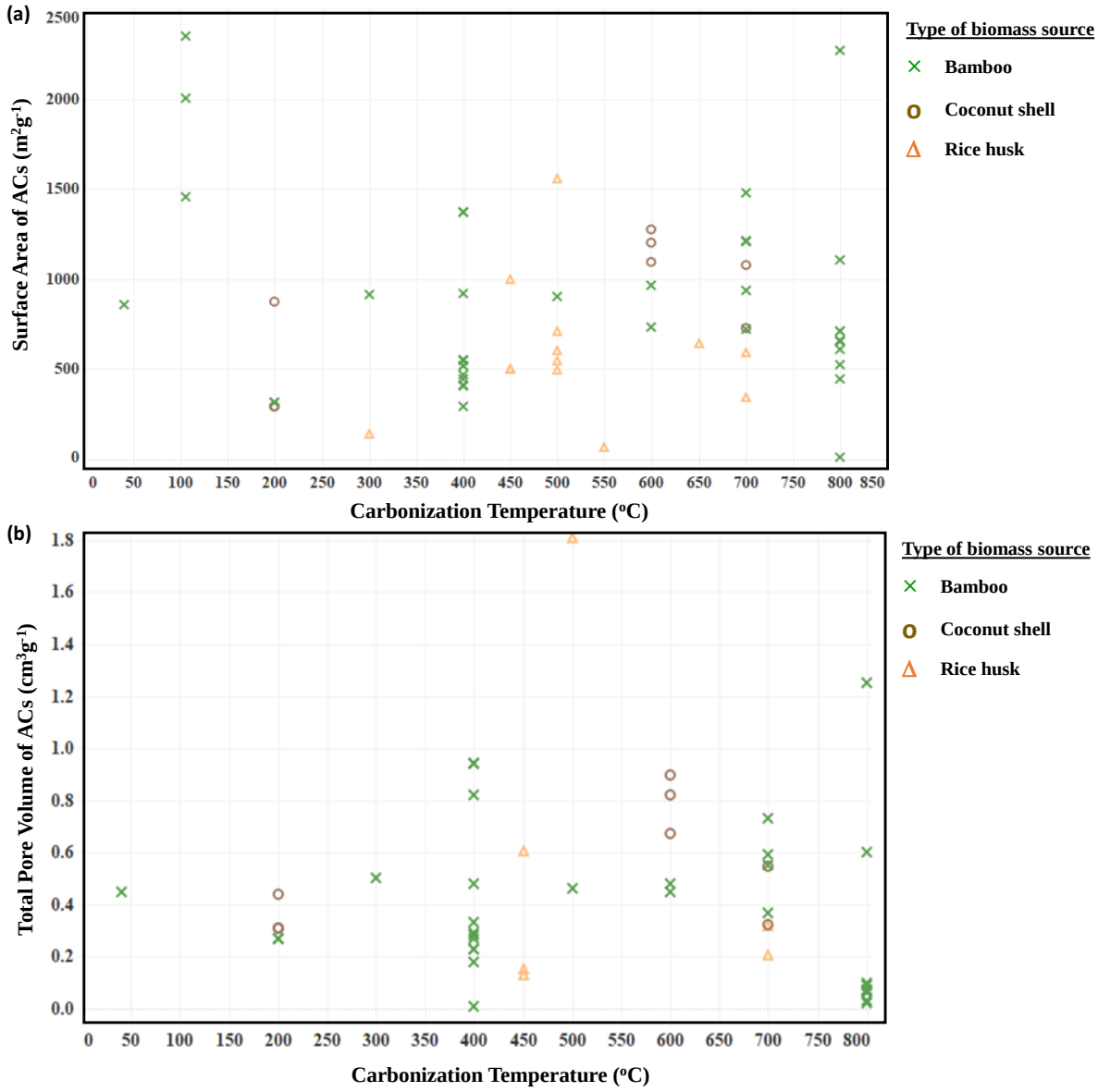


**Fig. 2:** Graph of (a) surface area of ACs versus carbonization temperature and (b) total pore volume of ACs versus carbonization temperature.

Results in Fig. 3(a-b) also show no significant changes in the surface area of rice husk AC when the carbonization process performed for 1 hour and 5 hours. Both holding times resulted in surface areas ranging from 300 $m^2g^{-1}$ to 700 $m^2g^{-1}$. However, the holding time could be kept as low as 0.5 hours yet still yielding twice as higher surface area and pore volume beyond 1500 $m^2g^{-1}$ and 1.8 $cm^3g^{-1}$, respectively, when the rice husk was impregnated with $H_3PO_4$ during chemical activation. The surface area and pore volume of the rice husk ACs also increase with the increase in the impregnation ratio ($H_3PO_4$: Rice Husk) from 3:1 to 5:1, highlighting the chemical agent impregnation ratio as a potential external factor that improved rice husk's physicochemical

properties [35,37]. The holding time of 1 hour has yielded coconut shell ACs with surface areas of 700 to 1500 $m^2g^{-1}$ and pore volume of 0.5 to 1.00 $cm^3g^{-1}$, which is relatively higher than the average rice husk and bamboo values ACs. In general, higher holding time increases the surface area and volume ratio due to more extended carbonization reactions occurring to the biomass. However, a longer reaction time at a high-temperature carbonization process will increase the synthesis cost and operational hazards.

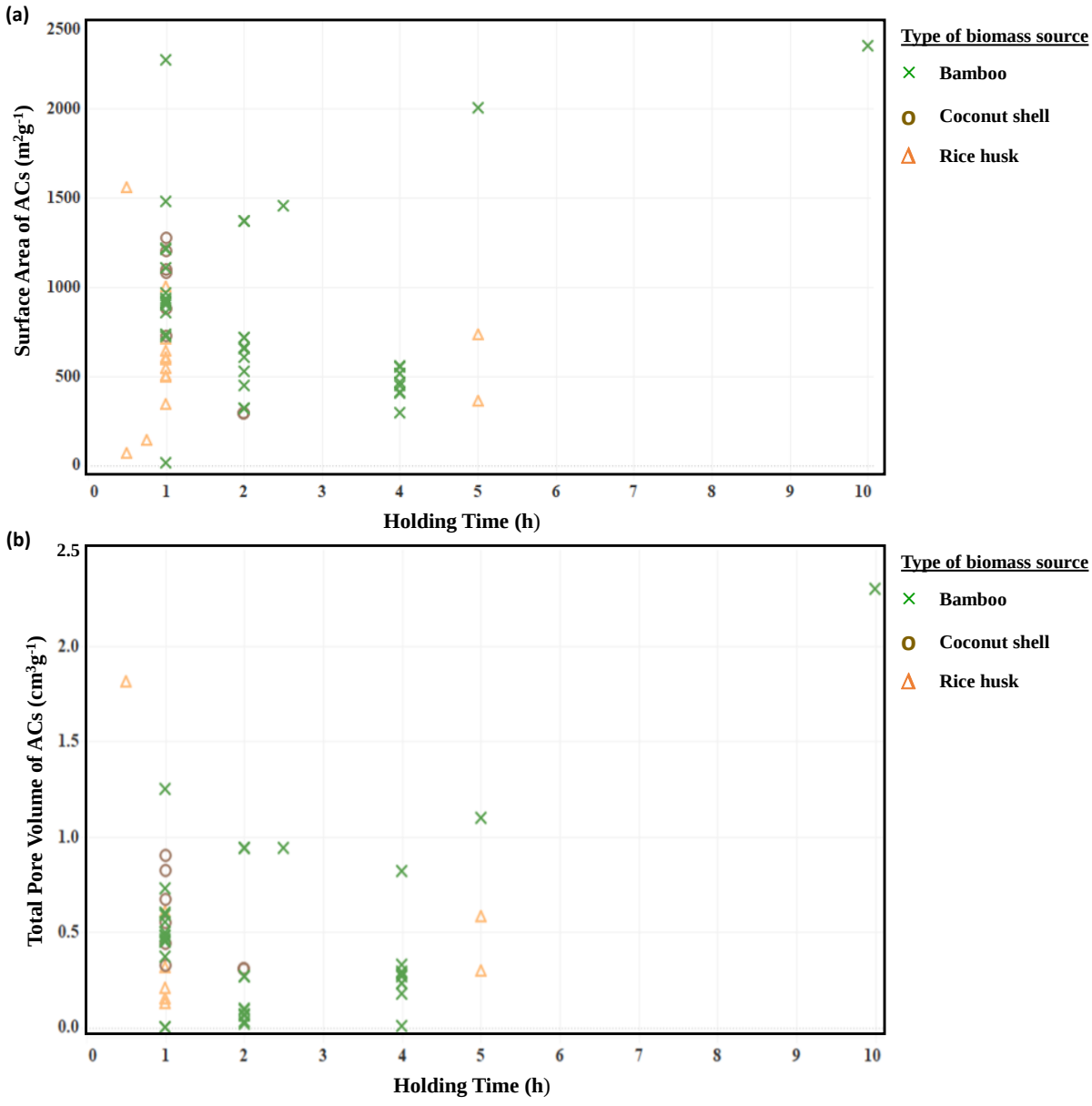


Fig. 3: Graphs of (a) surface area of ACs versus carbonization holding time and (b) total pore volume of ACs versus carbonization holding time.

The adsorption of MB is influenced by the adsorbent's properties and the adsorption conditions used during the adsorption process. Among the adsorption parameters, the dose of AC, initial concentration of the MB, and contact time are the parameters that were commonly varied and studied. They significantly influenced the adsorption properties of ACs. Therefore, the collected maximum dye removal (%) data were normalized in this study to ensure they are comparable across different published studies. The normalization was done by representing the percentage of MB removal data as percentage dye removal per dose of AC per dye concentration per contact time (% removal of MB (mg of AC)$^{-1}$ (mg/L of MB)$^{-1}$ h$^{-1}$). After data normalization, a more significant trend about the physicochemical properties to the performance of ACs could be observed.

Based on the graphs in Fig. 4(a-b), the average range of maximum MB removal could be achieved by ACs produced from all three biomass sources falls within 0.2 to 2 % removal of MB (mg of AC)$^{-1}$ (mg/L of MB)$^{-1}$ h$^{-1}$ when the range of surface area and pore volume of the ACs obtained are between 12 to 2200 $m^2g^{-1}$ and 0.07 to 1.25 $cm^3g^{-1}$ respectively. Within the average range, the dye adsorption capability towards MB increased with the increase of surface area and pore volume, indicating the favorability towards developing these two properties (surface area and pore volume) for improved MB adsorption. Higher surface area increases the adsorbents' available adsorption sites, which would allow more dye particles to adsorb onto its surface, thus increasing the dye removal capability from the wastewater.

Furthermore, according to Fig. 4a for bamboo ACs, the percentage removal could be drastically increased up to 10.0 % removal of MB (mg of AC)$^{-1}$ (mg/L of MB)$^{-1}$ h$^{-1}$ even at a relatively lower surface area of 734 $m^2g^{-1}$ when the bamboo was steam activated. This is because steam activation slightly decreased the content of acidic groups and slightly increased the range of primary groups, which later increased the pH. When steam-activated, the essential nature of the ACs indicates its potential application when the primary groups are desired, such as in the adsorption of cationic dyes like MB [53]. This observation agreed with the information reported by Zhang et al. (2014) where higher pH is preferable during MB adsorption [54]. More cationic dyes could be adsorbed onto the surface of ACs due to less competition with the $H^+$ ions at higher pH.

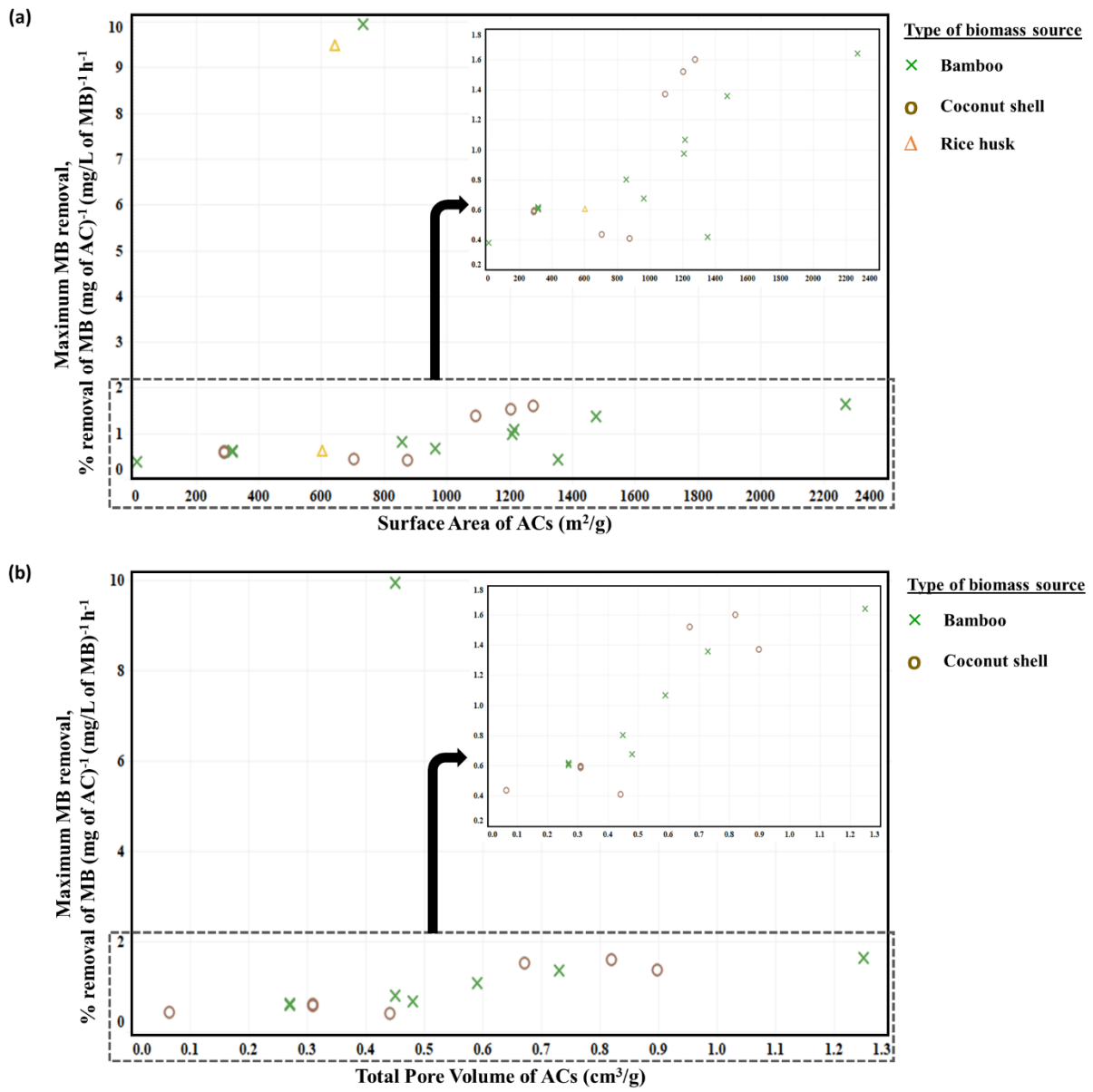


**Fig 4.** (a) Graph of maximum MB removal per dose of ACs per dye concentration per contact time versus the surface area of AC with an inset for the range of removal 0.2 to 1.8 % removal of MB (mg of AC)$^{-1}$ (mg/L of MB)$^{-1}$ h$^{-1}$, and (b) graph of maximum MB removal per dose of ACs per dye concentration per contact time versus the pore volume of ACs with an inset for the range of removal 0.2 to 1.8 % removal of MB (mg of AC)$^{-1}$ (mg/L of MB)$^{-1}$ h$^{-1}$.

Within the same range of surface area and pore volume, a similar trend in the percentage dye removal could be observed on coconut shell ACs. As mentioned previously, the surface area and the pore volume of coconut shells have been shown to be similar to that of bamboo ACs, although restricted to the carbonization temperatures of 600 - 700 $^{o}$C. Furthermore, higher percentage dye removal may be achieved beyond 10.0 % removal of MB (mg of AC)$^{-1}$ (mg/L of MB)$^{-1}$ h$^{-1}$ at higher

surface area and pore volume using different activating agents during the chemical activation step, such as monoethanolamine [12]. Monoethanolamine increased the AC's surface alkalinity when nitrogen functional groups in the amine solution were introduced [12]. The surface treatment using a basic chemical agent is necessary to significantly enhance the MB adsorption onto the surface of coconut ACs.

According to Fig. 4a, for the rice husk ACs, the percentage of MB removal significantly increased from 0.6 to 9.5 % removal of MB (mg of AC)$^{-1}$ (mg/L of MB)$^{-1}$ h$^{-1}$ with a slight difference in surface area (603 - 645 $m^2g^{-1}$). The significant improvement in its adsorption capability, even with a slight increase in surface area, was achievable when the pH of the solution was kept between pH 8 to 11. At higher pH, the surface of the rice husk ACs became negatively charged, which increases the adsorption of the positively charged MB through electrostatic force attraction [55]. Furthermore, the higher surface area of rice husk up to 645 $m^2g^{-1}$ ACs resulted from $ZnCl_2$ activation. Although rice husks carbonized at higher temperatures (>500$^o$C) could destroy its pore structure, incorporating $ZnCl_2$ could overcome this problem. Instead, well-developed pores with a good porous structure were formed, thus increasing the surface area that provided higher adsorption sites for more dye adsorption [43].

## 4. Conclusions and Future Outlook

The surface area and the pore volume of the ACs were observed to be among the critical physicochemical properties that majorly influence the ACs' adsorption performance towards MB. With the increase in surface area and pore volume, a higher percentage of MB could be removed from the wastewater. These properties could be manipulated by applying different carbonization temperatures and holding times during the AC synthesis. It was observed that both bamboo and coconut shells could achieve similar ranges of surface area and pore volume of 500 to 1500 $m^2g^{-1}$ and 0.2 to 1.0 $cm^3g^{-1}$, respectively. However, the coconut shell's carbonization temperature is more limited in the range of 600-700 $^o$C than the bamboo, with a broader range of 40-800 $^o$C. When the two were compared, the percentage removal achieved by both ACs showed similar distribution across the surface area and pore volume. However, lower temperatures less than 500$^o$C should be maintained for rice husks due to its AC structure that tends to be destroyed at higher temperatures. The holding time did not significantly impact rice husk and coconut shell ACs and was commonly sufficient to be kept at 1 hour. Meanwhile, bamboo ACs had higher surface area and pore volume

with a longer holding time. Furthermore, the three biomasses were seen to have significant improvements in dye removal through surface modification through steam activation, chemical activation, and alkaline pH.

Some potential areas surrounding ACs could be highlighted for future research, among the information gathered during the systematic literature review. For example, the regeneration of AC is one of the most critical aspects of its usage in adsorptive applications. The current industrial enterprises and municipalities using commercialized ACs require renewal and reactivation as feasible solutions to decrease carbon footprints and production costs. However, the studies from the research papers lack the information on the reusability for ACs synthesized from these biomasses, which could be further explored and beneficial to be included as part of the ACs' development for contaminant removal and commercialization potential.

**Conflicts of interest**

There are no conflicts to declare

**Acknowledgments**

R.R. Nasaruddin would like to acknowledge the financial support from the Ministry of Higher Education Malaysia under research grant (FRGS-RACER/1/2019/TK02/UIAM//1) for the study.

Electronic Supplementary Information (ESI) available: See DOI: 10.1039/x0xx00000x

**References**

1. Regti, A., Laamari, M. R., Stiriba, S.-E., El-Haddad, M., The potential use of activated carbon prepared from *Ziziphus* species for removing dyes from waste waters, *Appl. Water Sci.*, **2017**, 7(7), 4099–4108.

2. Sahu O, Singh N, Significance of bioabsorption process on textile industry wastewater. In the Impact and Prospects of Green Chemistry for Textile Technology, By ul-Islam S., Butola B.S. (Eds), The Textile Institute Book Series, *Woodhead Publishing*, **2019**, 367-416,

3. Benedetti, V., Patuzzi, F., Baratieri, M. (2018). Characterization of char from biomass gasification and its similarities with activated carbon in adsorption applications. *Appl. Energy*, **2018**, 227, 92–99.

4. Chowdhury, Z. Z., Hamid, S. B. A., Das, R., Hasan, M. R., Zain, S. M., Khalid, K., Uddin, M. N., Preparation of carbonaceous adsorbents from lignocellulosic biomass and their use in removal of contaminants from aqueous solution. *BioResources,* **2013**. 8(4), 6523–6555.

5. Afif, A., Rahman, S. M., Tasfiah Azad, A., Zaini, J., Islan, M. A., Azad, A. K., Advanced materials and technologies for hybrid supercapacitors for energy storage – A review. *J. Energy Storage* **2019**, 100852.

6. Widiyastuti, W., Fahrudin Rois, M., Suari, N. M. I. P., Setyawan, H., Activated carbon nanofibers derived from coconut shell charcoal for dye removal application. *Adv. Powder Technol.* **2020**, 31(8), 3267–3273.

7. Ogata, F., Yasuda, S., Saenjum, C., Nakamura, T., Kawasaki, N., Interactions of cationic and anionic dyes with activated carbons. *E-J. Surf. Sci. and Nanotechnol*. **2020**, 18, 269–274.

8. Nainamalai, M., Palani, M., Allwin Ebinesar, J. S. S., Bhuvaneshwari, S., Decolorization of anionic and cationic dyes by electro-adsorption process using activated carbon electrodes. *Indian J. Chem.* **2019**, 26(4), 300–311.

9. Khuluk, R. H., Rahmat, A., Buhani, B., Removal of methylene blue by adsorption onto activated carbon from coconut shell (*Cocous Nucifera L*.). *Indones. J. Sci. and Technol*. **2019**, 4(2), 229–240.

10. Regunton, P. C. V., Sumalapao, D. E. P., Villarante, N. R., Biosorption of methylene blue from aqueous solution by coconut (*Cocos nucifera*) shell-derived activated carbon-chitosan composite. *Orient. J. of Chem.* **2018**, 34(1), 115–124.

11. Islam, M. A., Ahmed, M. J., Khanday, W. A., Asif, M., Hameed, B. H., Mesoporous activated coconut shell-derived hydrochar prepared via hydrothermal carbonization-NaOH activation for methylene blue adsorption. *J. Environ. Manage.* **2017**, 203, 237–244.

12. Das, D., Meikap, B. C., Optimization of process condition for the preparation of amine-impregnated activated carbon developed for $CO_2$ capture and applied to MB adsorption by response surface methodology. *J. Environ. Sci. Health A* **2017**, 52(12), 1164–1172.

13. Vi, N. N. T., Truyen, D. H., Trung, B. C., An, N. T., Van Dung, N., Long, N. Q., Porous carbon from local coconut shell char by $CO_2$ and $H_2O$ activation in the presence of $K_2CO_3$. *AIP Conf. Proc*. **2017**, 1878.

14. Sanni, E. S., Emetere, M. E., Odigure, J. O., Efeovbokhan, V. E., Agboola, O., Sadiku, E. R., Determination of optimum conditions for the production of activated carbon derived from separate varieties of coconut shells. *Int. J. Chem. Eng.* **2017**. 2801359.

15. Yasin, J., & Pravinkumar, R., Production of activated carbon from bio-waste materials by chemical activation method. *AIP Conf. Proc.* **2020**, 2225.

16. Bokil, S. A., Topare, N. S., Khedkar, S. V., Batch Adsorption Studies on Treatment of Textile Industry Effluent using Bamboo and Green Coconut shell Activated Carbon. *IOP Conf. Ser.: Mater. Sci. Eng.* **2020**, 983, 012005.

17. Van, H. T., Nguyen, T. M. P., Thao, V. T., Vu, X. H., Nguyen, T. V., Nguyen, L. H., Applying Activated Carbon Derived from Coconut Shell Loaded by Silver Nanoparticles to Remove Methylene Blue in Aqueous Solution. *Water Air Soil Pollut.* **2018**, 229, 393.

18. Efeovbokhan, V. E., Alagbe, E. E., Odika, B., Babalola, R., Oladimeji, T. E., Abatan, O. G., Yusuf, E. O., Preparation and characterization of activated carbon from plantain peel and coconut shell using biological activators. *J. Phys. Conf. Ser.* **2019**, 1378, 032035.

19. Ali, A. F., Kovo, A. S., Adetunji, S. A. (2017). Methylene Blue and Brilliant Green Dyes Removal from Aqueous Solution Using Agricultural Wastes Activated Carbon. *J. Encapsulation Adsorp. Sci.* **2017**, 07(02), 95–107.

20. Sangotayo, E. O. (2018). Thermal Evaluation of Some Locally Produced Activated Carbon from Agricultural Residue. *J. Nat. Sci. Res.* **2018**, 8(18), 23–31.

21. Abdullah, N. H., Inu, I., Razab, M. K. A. A., Noor, A. M., Zaudin, N. A. C., Rasat, M. S. M., Amin, M. F. M., Abdullah, W. N. W., Shukri, N. M., Halim, A. Z. A., Effect of Acidic and Alkaline Treatments to Methylene Blue Adsorption from Aqueous Solution by Coconut Shell Activated Carbon. *Int. J. Current Res. Sci. Eng. Technol.* **2018**, 319–324

22. Machdar, I., Faradillasari, C., Khair, N. A., Asnawi, T. M., BC, A. Y., Yunardi, Y., Effects of $Fe^{2+}$ and $Fe^{3+}$ ratio impregnated onto local commercial activated carbon coconut shell powder on the dye removal efficiency. *Jurnal Litbang Industri* **2018***,* 8(1), 11–16.

23. Ma, X., Smith, L. M., Cai, L., Shi, S. Q., Li, H., Fei, B. Preparation of high-performance activated carbons using bamboo through one-step pyrolysis. *BioResources* **2019**, 14(1), 688–699.

24. Santana, G. M., Trugilho, P. F., Da Silva Borges, W. M., Bianchi, M. L., Paes, J. B., Nobre, J. R. C., De Medeiros Morais, R., Activated carbon from bamboo (*bambusa vulgaris*) waste using $CO_2$ as activating agent for adsorption of methylene blue and phenol. *Ciênc. Florest.* **2019**, 29(2), 769–778.

25. Jawad, A. H., Abdulhameed, A. S., Statistical modeling of MB adsorption by high surface area mesoporous activated carbon from bamboo chip using KOH-assisted thermal activation. *Energy Ecol. Environ.* **2020**, 5(6), 456–469.

26. Efiyanti, L., Indrawan, D. A., Hastuti, N., Darmawan, S., The activated carbon produced from mayan bamboo (*Gigantochloa robusta Kurz*) and its application as dye removal. *IOP Conf. Ser.: Mater. Sci. Eng.* **2020**, 935, 012018.

27. Mi, B., Wang, J., Xiang, H., Liang, F., Yang, J., Feng, Z., Zhang, T., Hu, W., Liu, X., Liu, Z., Fei, B., Nitrogen self-doped activated carbons derived from bamboo shoots as adsorbent for methylene blue adsorption. *Molecules* **2019,** 24(16). 3012.

28. Zhang, Q., Zeng, Y., Xiao, X., Deng, P., He, Q., Zhang, T., Investigation on the Preparation and Adsorption Performance of Bamboo Fiber Based Activated Carbon. *Fibers Polym.* **2019**, 20(2), 293–301.

29. Chen, L., Ji, T., Mu, L., Shi, Y., Wang, H., Zhu, J. (2017). Pore size dependent molecular adsorption of cationic dye in biomass derived hierarchically porous carbon. *J. Environ. Manage.* **2017**, 196, 168–177.

30. Hata, M., Amano, Y., Thiravetyan, P., Machida, M., Preparation of Bamboo Chars and Bamboo Activated Carbons to Remove Color and COD from Ink Wastewater. *Water Environ. Res.* **2015**, 88(1), 87–96.

31. Tadesse, S., Ambo, D., Removal of Basic Dye from Aqueous Medium Using Activated Carbon from *Erythrina Brucei, Arundinaria Alpina* and *Manihot Esculenta*. *Food Sci. Qual. Manage.* **2019**, 86, 19–27.

32. Qanytah, Q. Syamsu, K., Fahma, F., Pari, G., Characterization of Ball-Milled Bamboo-Based Activated Carbon Treated with $KMnO_4$ and KOH as Activating Agents. In *BioResources* **2020**, 15(4), 8303–8322

33. Santana, G. M., Lelis, R. C. C., Paes, J. B., Morais, R. de-M., Lopes, C. R., de Lima, C. R., Activated Carbon from Bamboo (*Bambusa vulgaris*) for Methylene Blue Removal: Prediction to The Environment Applications. *Ciênc. Florest.* **2018**., 1179–1191.

34. Kibami, D., Comparative study of low-cost adsorbents prepared indigenously from locally available bio-waste for the removal of methylene blue dye. *J. Water Sci. Environ. Technol*. **2017**, 02, 213–225.

35. Li, Y., Pan, B., Miao, H., Xu, H., Liu, X., Shi, G., Single and Binary Dye Adsorption of Methylene Blue and Methyl Orange in Alcohol Aqueous Solution via Rice Husk Based Activated Carbon: Kinetics and Equilibrium Studies. *Chem. Res. Chinese U.* **2020**, 36(6), 1272–1278.

36. Alver, E., Metin, A. Ü., Brouers, F. (2020). Methylene blue adsorption on magnetic alginate/rice husk bio-composite. *Int. J. Biol. Macromol.* **2020**, 154, 104–113.

37. Basta, A. H., Lotfy, V. F., Hasanin, M. S., Trens, P., El-Saied, H., Efficient treatment of rice byproducts for preparing high-performance activated carbons. *J. Clean. Prod.* **2019**, 207, 284–295.

38. Liou, T. H., Wang, P. Y., Utilization of rice husk wastes in synthesis of graphene oxide-based carbonaceous nanocomposites. *Waste Manage.* **2020**, 108, 51–61.

39. Kaykioğlu, G., Güneş, E., Kinetic and equilibrium study of methylene blue adsorption using H2SO4− activated rice husk ash. *Desalin. Water Treat.* **2016**, 57(15), 7085–7097.

40. Thambiliyagodage, C. J., Cooray, V. Y., Perera, I. N., Wijesekera, R. D., Eco-Friendly Porous Carbon Materials for Wastewater Treatment. *In Lecture Notes in Civil Engineering* **2020**, 44, Springer Singapore.

41. Nworie, F. S., Nwabue, F. I., Oti, W., Mbam, E., Nwali, B. U., Removal of methylene blue from aqueous solution using activated rice husk biochar: Adsorption isotherms, kinetics and error analysis. *J. Chil. Chem. Soc.* **2019**, 64(1), 4365–4376.

42. Ahmad, T., Promi, S. i., Rumpa, I. J., Color Removal from Tannery Wastewater Using Activated Carbon Generated from Rice Husk, *World Environmental and Water Resource Congress* **2018.** 489.

43. Desalgne, A., Optimal Removal of Methylene Blue in Aqueous Solution Using Selected Rice Husk Activated Carbon from Pore Development. *Thesis* **2019**. Addis Ababa University, Ethiopia.

44. Ahmad, M. A., Basir, N. I., Yahaya, N. K. E., Microwave assisted rice husk based activated carbon for adsorption of methylene blue. *Int. J. Petrochemistry Res*. **2018,** 2(2), 162–164.

45. Murat, M., Ahmad, M. A., Idris, M. N., Optimization of preparation conditions for rice husk based activated carbons for the removal of methylene blue. *Int. J. Petrochemistry Res.* **2018**, 2(2), 186–188.

46. Ma, H. T., Ly, H. C., Ho, V. T. T., Pham, N. B., Nguyen, D. C., Vo, K. T. D., Tuan, P. D., Effect of the Carbonization and Activation Process on the Adsorption Capacity of Rice Husk Activated Carbon. *Vietnam J. Sci. Technol.* **2017**, 55(4), 494–502.

47. Bahago, N. A., Sorption Studies of Methylene Blue Using Activated Carbon Produced from Rice Husk., *Commun. Phy. Sci*. **2018**, 3, 91–96.

48. Ahiduzzaman, M., Sadrul Islam, A. K. M. Preparation of porous bio-char and activated carbon from rice husk by leaching ash and chemical activation. *SpringerPlus* **2016**, 5, 1248.

49. Radenahmad, N., Azad, A. T., Saghir, M., Taweekun, J., Bakar, M. S. A., Reza, M. S., Azad, A. K., A review on biomass derived syngas for SOFC based combined heat and power application. *Renew. Sust. Energ. Rev.* **2020**, 119, 109560.

50. Alhinai, M., Azad, A. K., Bakar, M. S. A., Phusunti, N., Characterisation and thermochemical conversion of rice husk for biochar production. *Int. J. Renew. Energy Res.* **2018**, 8(3), 1648–1656.

51. Ao, W., Fu, J., Mao, X., Kang, Q., Ran, C., Liu, Y., Zhang, H., Gao, Z., Li, J., Liu, G., Dai, J., Microwave assisted preparation of activated carbon from biomass: A review. *Renew. Sust. Energ. Rev.* **2018**, 92, 958–979.

52. Reza, M. S., Yun, C. S., Afroze, S., Radenahmad, N., Bakar, M. S. A., Saidur, R., Taweekun, J., Azad, A. K., Preparation of activated carbon from biomass and its' applications in water and gas purification, a review. *Arab J. Basic Appl. Sci.* **2020**, 27(1), 208–238.

53. Zhang, Y. J., Xing, Z. J., Duan, Z. K., Li, M., Wang, Y., Effects of steam activation on the pore structure and surface chemistry of activated carbon derived from bamboo waste. *Appl. Surf. Sci* **2014**, *315*(1), 279–286.

54. Kuang, Y., Zhang, X., Zhou, S., Adsorption of methylene blue in water onto activated carbon by surfactant modification. *Water (Switzerland)* **2020**, *12*(2), 1–19.

55. Kaykioğlu, G., Güneş, E., Kinetic and equilibrium study of methylene blue adsorption using $H_2SO_4$−activated rice husk ash. *Desalin. Water Treat.* **2016**, 57(15), 7085–7097.

Malaysian Catalysis-An International Journal

*Malay. Catal.Int.J Vol 1, Issue 2(2021) 31-41*

## RESEARCH ARTICLE

# Synergistic effect of Promoter addition and Nickel Loading for Catalysed Dry Reforming of Methane

Received 21st Dec 2021,
Revised 24th Feb 2022,
Accepted 25th Feb 2022

DOI: 10.22452/mcij.vol1no2.3

*Corresponding author*:
durgadevi@um.edu.my

Durga Devi Suppiah [a], Radziah Sa'arani [a], and Mohd Rafie Johan [a].

[a] Nanotechnology & Catalysis Research Centre (NANOCAT), University of Malaya, Kuala Lumpur,

**Abstract**

This paper investigates the synergistic influence of both catalyst active sites Lanthanum promoter and Nickel loading on supported Ni catalysts for Dry Reforming of Methane (DRM) reaction. Alumina-supported nanosized Ni-based catalysts were synthesized using the impregnation method with varying percentages of Lanthanum promoter. Structural analysis via XRD, SEM and PSD show Nickel and lanthanum particles were homogeneously dispersed on $Al_2O_3$ supported catalyst with a size range of 40-90 nm were obtained. Lanthanum addition favors equilibrated reaction equivalent to the DRM mechanism. Increasing the La percentage and temperature however shifts the equilibrium to a higher conversion of $CH_4$ (72%) hence higher H2 selectivity (70%).

*Keywords*: Greenhouse gases; CO2 Utilization; Dry Reforming Methane; Catalyst

## 1.0 Introduction

Natural Gas utilization is the main source of energy in Malaysia with the largest natural gas reservoir in South East Asia. Recent studies estimate that burning 1 ton of carbon in fossil fuels produces above 3.5 tons of $CO_2$. Current carbon capture and storage (CCS) technologies focus mainly on capture from large intensive sources such as oil refineries and power plants. $CO_2$ disposal by sequestration in geological storage has been costly and possess some limitation such as leakage, storage capacity, and also operation and maintenance cost. However, the continuous development of this high $CO_2$ gas field has created a significant new challenge whereby the paradigm has shifted from Carbon Capture Sequestration (CCS) to Carbon Capture Utilization (CCU) [1-3]. The valorization of methane to liquid fuels has been extensively studied due to large volumes of methane resources. Methane which is a major component of natural gas is produced at

the offshore reservoir, hence transportation is a hassle. Dry Reforming of Methane combines the utilization of both $CO_2$ and $CH_4$ to produce syngas which is used extensively for conversion to value-added products. Nevertheless, the challenge arises from catalyst design and development as a high temperature (>700 °C) is needed for this highly endothermic reaction [3, 4]. Currently, available catalysts are noble metal catalysts such as Ru, Rh, and Pt due to their high activity and susceptibility to deactivation [5]. Nevertheless, current research is more leaning towards supported Nickel and Copper-based catalyst as they are preferred in the industry as it is cheaper and has comparable activity [6]. However, the major setback from this reaction is rapid catalyst deactivation due to coke formation from CO continuous disproportionation reaction which leads to catalyst sintering[7, 8]. To avoid this, an alkaline promoter was added to reduce carbon deposition. La promoter can reduce sintering by mesoporous framework confinement besides increasing the basic site. Coke deposition can also be reduced if the reaction temperature can be reduced [9]. Synthesis parameters play a major role in obtaining the suitable catalyst structure and morphology for the desired reaction [10, 11]. In this manuscript, the role of La promoter and Nickel loading along with the reaction parameters will be scrutinized to further understand the mechanism of DRM for further catalysts upgrading.

## 2.0 Materials and Methods

### 2.1 Catalyst Synthesis & Characterization

A series of Nickel (Ni) catalysts supported on Alumina was synthesized at 30 °C using the impregnation method. 5g of Aluminum oxide was added slowly to 100 ml of Nickel (II) chloride solution (5, 10 & 50 wt% Ni) while stirring. Lanthanum oxide was added as the same amount percentage as nickel. The solution was allowed to stir continuously for 1 hour and then evaporated to dryness at 80 °C. The solid powder obtained was dried in an oven at 60 °C for 24 hours to remove the excess water. The X-Ray Diffractograms (XRD) were obtained using a Bruker's Theta/2theta goniometer and a Scintillation counter detector. The data sets were collected in reflection geometry in the range of $2° \leq 2\theta \leq 80°$ with a step size of $\Delta 2\theta = 0.02°$ analyzed using High Score Plus software for phase identification. The surface morphology and the particle size distribution were determined using FEI's Field Emission Scanning Electron Microscope-Energy Dispersive X-ray (FESEM-EDX) and Malvern's Zetasizer. The synthesized catalysts were then activated in a tubular furnace underflow of 20ml/min of synthetic air.

### 2.2 Catalyst Activity Evaluation

Prior to the reaction, the synthesized catalyst was reduced based on Temperature Programmed Reduction conducted in Thermo Finnigan's TPDRO 1100. The catalytic activity for Dry Reforming of Methane was evaluated in a fixed bed reactor (Nanoflow) equipped with a valve switching gas chromatographic system for a quantitative effluent gas analysis. 0.3 g of catalyst were loaded into each reactor tube and the volume of the catalyst bed was set at 5 ml by inert (SiC) packing. The flow rate of the reactant feed was set to 100 ml/min ($N_2/CO_2/CH_4$ = 80:10:10) and GHSV 10,000 $h^{-1}$) into the reactor tube at a temperature range of 450 - 525 °C. The spent catalysts were sieved to separate the SiC packing particles and subjected again to XRD and PSD analysis.

## 3. Results & Discussion

### 3.1 Structural Properties of Synthesized Catalyst

Figure 1 shows the XRD Diffractograms of synthesized Ni-based nanocatalyst with high crystallinity. All diffractograms show peak characteristics indexed to Nickel Oxide, NiO, a cubic phase, (PDF File 022-1189) with prominent peaks matching at 37.3° (003), 43.3° (012) and 62.9° (110) though it appears to be shifted in Figure 1 (b). Figure 1 (b,c,d) exhibits the addition of $La_2O_3$ matching the diffractogram with Lanthanum oxide, cubic crystal structure (PDF File 040-1284) with prominent peaks at 28.0°, (110) 39.8 (002) and 49.2° (211) though peaks at 28 and 49.2° appear to be overlapping with Lanthanum Nickel Oxide (PDF File 089-1029). This may be due to the composite formed when $La_2O_3$ was used as support. There is an additional peak at 16° indexed to Lanthanum Hydroxide, La $(OH)_3$ (PDF File 075-1900). The addition of lanthanum did not alter the phase diffractogram drastically suggesting that there is no alteration to the crystal structure. Another match in Figure 1 (a,c,d) was the support used which is Aluminium Oxide, $Al_2O_3$, rhombohedral phase, (PDF File 071-1124) with prominent peak matches at 25.6° (012), 35.2° (104), 43.4° (113) and 57.6° (116). No residue of used ligand was observed confirming pure phase synthesized nanocatalyst. SEM imaging with EDX mapping in Figure 2 shows the Nickel and $La_2O_3$ particles were homogeneously dispersed which will enable strong interaction with the Aluminium oxide support [6].

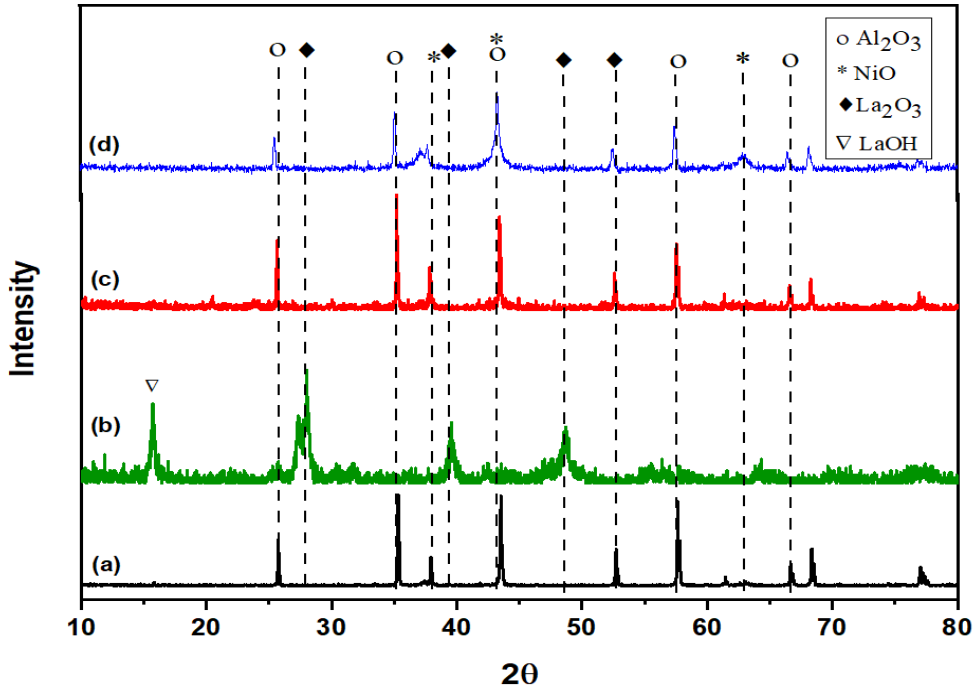


**Figure 1**: X-Ray powder diffractogram of synthesized (a)5% Ni/$Al_2O_3$ (b) 5% Ni/$La_2O_3$ (c) 10% Ni/La/$Al_2O_3$ (d) 50% Ni/La/$Al_2O_3$

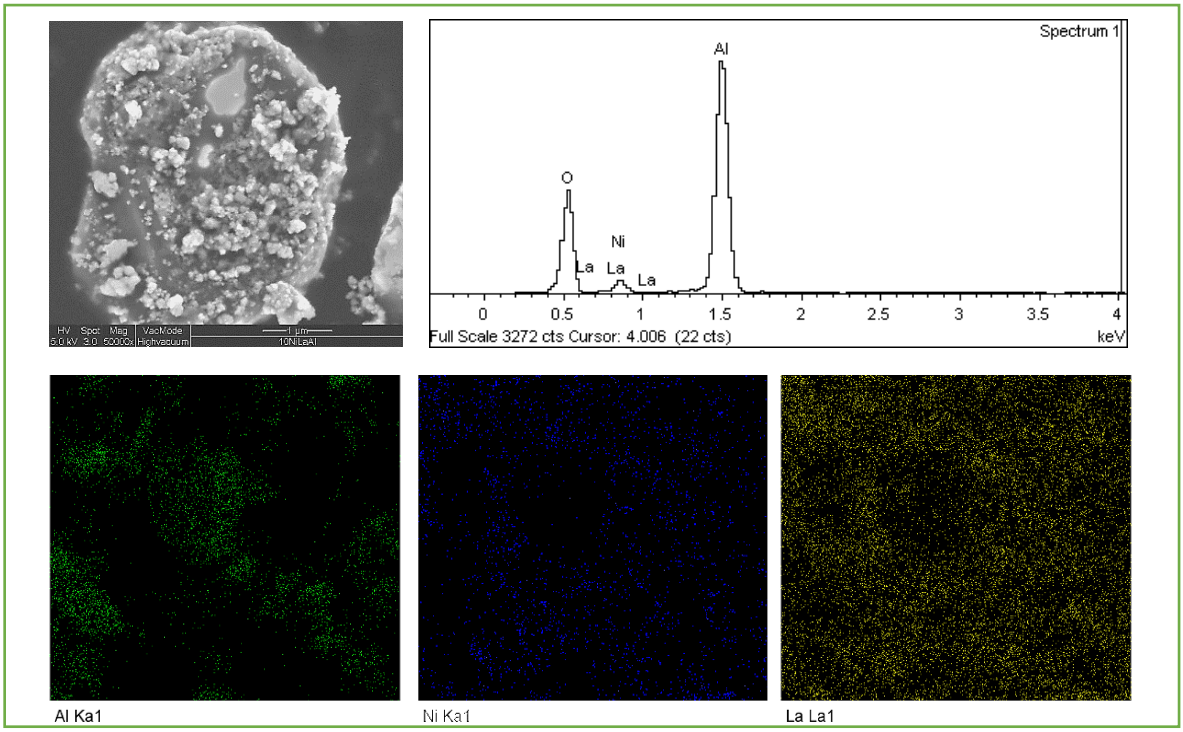


**Figure 2**: SEM - EDX mapping of synthesized 10% Ni/La/$Al_2O_3$

Particle size distribution (PSD) analysis shown in Table 1 shows that all synthesized Ni-based catalysts are within the nano range. This is essential for higher catalytic surface activity. Unsupported 5% Ni/$La_2O3$ catalyst (Figure 3(b)) exhibits the smallest particle size with the mean range obtained was 42 nm while the mode of particle size was in the range of 33-38 nm. The addition of Alumina support increases the particle size to a mean average of 80 nm for both 5% Ni/$Al_2O_3$ and 10% Ni/La/$Al_2O_3$. 50% Ni/La/ $Al_2O_3$ exhibits the largest particle size among all synthesized catalysts with an average size of 95 nm.

**Table 1.** Catalyst Particle Size Distribution (PSD) before & after DRM reaction.

| **Catalyst** | **Pre-Reaction Size (nm)** | | **Post Reaction Size (nm)** | |
|---|---|---|---|---|
| | **Mode** | **Mean** | **Mode** | **Mean** |
| 5% Ni/$Al_2O_3$ | 60-90 | 80 | 141-190 | 173 |
| 5% Ni/$La_2O_3$ | 33-38 | 42 | 68-92 | 82 |
| 10% Ni/La/$Al_2O_3$ | 68-91 | 79 | 122-164 | 161 |
| 50% Ni/La/$Al_2O_3$ | 78-105 | 95 | 140-191 | 150 |

### 3.2 Catalyst Activation Profile

TPR Profile shown in Figure 4 shows Ni is reduced at a lower temperature (400 °C) compared to the support & promoter used. Two distinct humps were observed indicating the Nickel active component was reduced in two stages as seen in Equation (1)

$$Ni^{2+} \rightarrow Ni^{1+} \rightarrow Ni^{0} \text{ - - - - - - - - - - - - - (1)}$$

However, the TPR profile of 5% Ni/$La_2O_3$ shows another distinct hump at 693 °C which maybe the reducing temperature of Lanthanum Oxide ($La_2O_3$). The presence of La also shifted the $Ni^{1+}$ reduction peak to a slightly higher temperature from 400 °C to 450 °C, perhaps due to the formation of mixed nickel lanthanum oxides [12]. Hence, a longer reduction holding time is required for this catalyst. The inert alumina support is incredibly thermally stable and does not react in any way with the active component hence providing a stable base for nickel catalyst. This is an attractive alternative catalyst next to the expensive ruthenium-based catalyst.

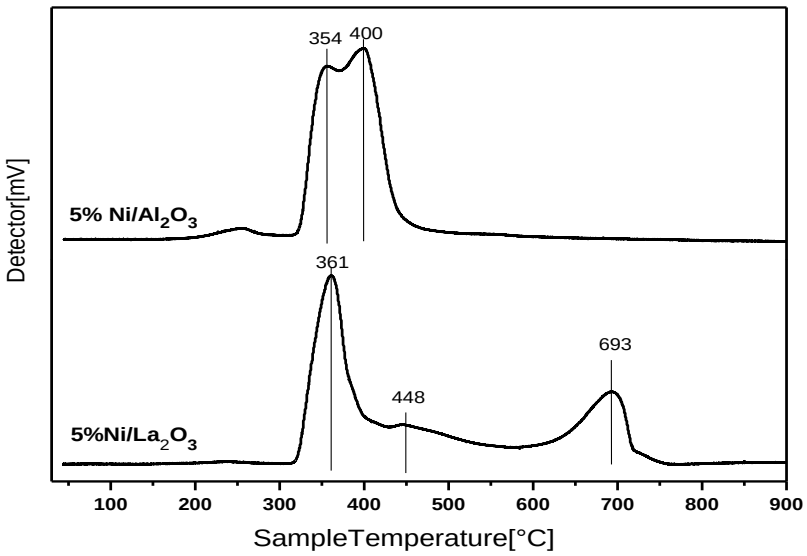


**Figure 4:** Temperature Programmed Reduction (TPR) of the synthesized catalyst

### 3.3 Dry Reforming of Methane Catalyst Activity Studies

**Table 2**: Catalytic performance of different Ni loading catalysts for DRM

| Catalyst | Temperature (°C) | Conversion ($XCO_2$ %) | Conversion ($XCH_4$ %) | Selectivity ($SH_2$%) | Selectivity (SCO%) |
|---|---|---|---|---|---|
| Blank | 500 | 0 | 3.68 | 100 | 0 |
| | 525 | 1.65 | 0 | 100 | 0 |
| 5% $Ni/Al_2O_3$ | 500 | 19.28 | 86.97 | 65.96 | 34.04 |
| | 525 | 0 | *93.27 | *79.71 | *20.29 |
| 5% $Ni/La_2O_3$ | 500 | 42.30 | 40.28 | 44.24 | 55.76 |
| | 525 | 43.58 | 53.05 | 56.22 | 43.78 |
| 10% $Ni/La/Al_2O_3$ | 500 | 37.56 | 57.13 | 66 | 34 |
| | 525 | 50.52 | 61.14 | 56.75 | 43.25 |
| 50% $Ni/La/Al_2O_3$ | 500 | 39.93 | 50.85 | 56.93 | 43.07 |
| | 525 | 46.58 | 72.06 | 70.61 | 29.39 |

# Reaction conditions: 1.0 MPa, 100 ml/min ($N2/CO_2/CH_4$=80:10:10) and GHSV 10,000 $h^{-1}$
*Only 1 point of GC analysis were recorded

The Ni-based catalyst was reduced at 400 °C before DRM reaction to only reduce the $Ni^{2+}$ to $Ni^0$ since pure NiO surface is not active [13] without disruption to the structural integrity of $Al_2O_3$ and $La_2O_3$. To investigate the influence of lanthanum of the Dry Reforming of Methane, different

loading of Ni-based catalyst were evaluated against non-promoted Ni catalyst and also under blank conditions. The DRM mechanism is as follow (eq 2);

$$\mathbf{CO_2 + CH_4 \rightarrow 2CO + 2H_2}\text{----------}\mathbf{(2)}$$

Table 1 displays the normalized conversion percentage of $CO_2$ and $CH_4$ and also the selectivity to CO and $H_2$. There was no significant conversion observed for blank reaction (Figure 5). As shown in figure 4, non-promoted 5%$Ni/Al_2O_3$ favors the conversion of $CH_4$ and can reach a maximum conversion of 87% amounting to 66% $H_2$ selectivity at 500 °C. These findings are consistent with extensive studies done previously exhibiting Nickel supported on Alumina catalyst as a favorable catalyst for DRM mechanism though it is conducted at a much higher temperature [8, 14]. However, there was no activity observed after raising the temperature to 525°C. Alumina has a higher sintering rate via surface diffusion thus an immediate reaction halt was observed after raising the temperature [15]. This may be due to coke deposits due to the high conversion of methane hence eliminating the presence of oxygen vacancies which is crucial for the catalyst active sites surface activity [6]. With the addition of lanthanum, there is almost an equal balance of both $CO_2$ and $CH_4$ conversion aligning with the reaction equation (2) and this is prominent with 10% $Ni/La/Al_2O3$ catalyst. The selectivity of both $H_2$ and CO was also almost 50% matching the reaction stoichiometry of 1:1 ratio. By increasing the Nickel loading the selectivity shifted towards $H_2$. This may be caused by the larger particle size providing an increase of methane adsorption on the Ni surface [9]. At 525 °C, 50% $Ni/La/Al_2O3$ catalyst shows the highest conversion of $CH_4$ at 72%. The addition of lanthanum inhibits the sintering process of alumina by maintaining the reactive surface area sites by increasing the Ni confinement [16, 17]. However, the attempt to increase the temperature to 550 °C was halted as there was no reactant flow and no activity was recorded. It may be inferred that by raising the temperature, the CO formed to continue to combust causing coking inhibiting the active sites and porosity that subsequently have stopped the flow of reactant gas to the catalyst.

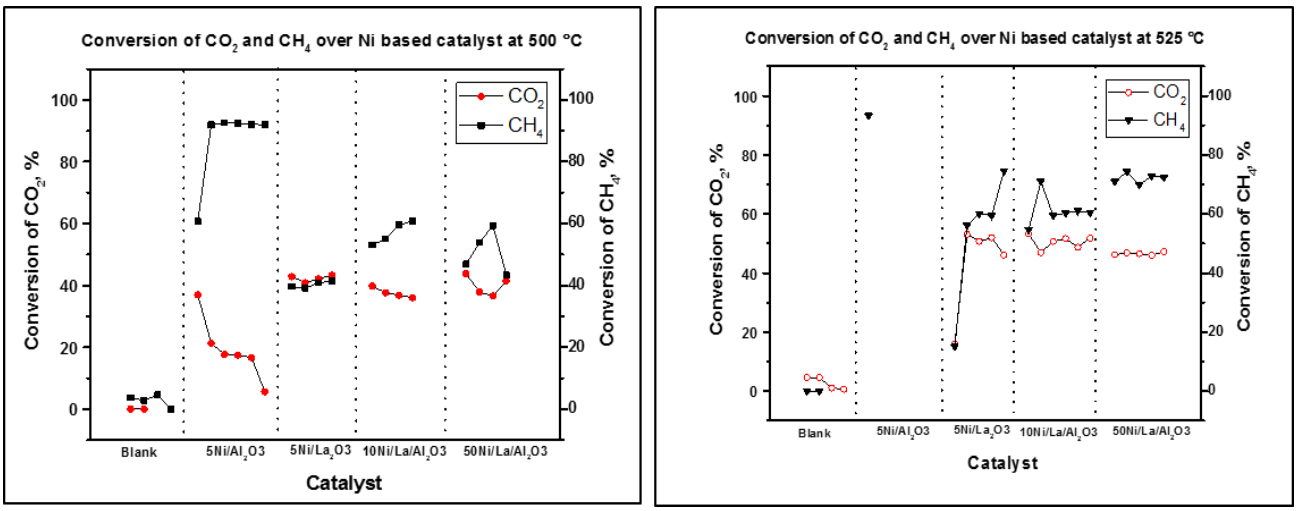


**Figure 5:** Catalytic conversion of $CO_2$ & $CH_4$ at (a) 500 °C (b) 525 °C

### 3.4 Post Reaction Characterization

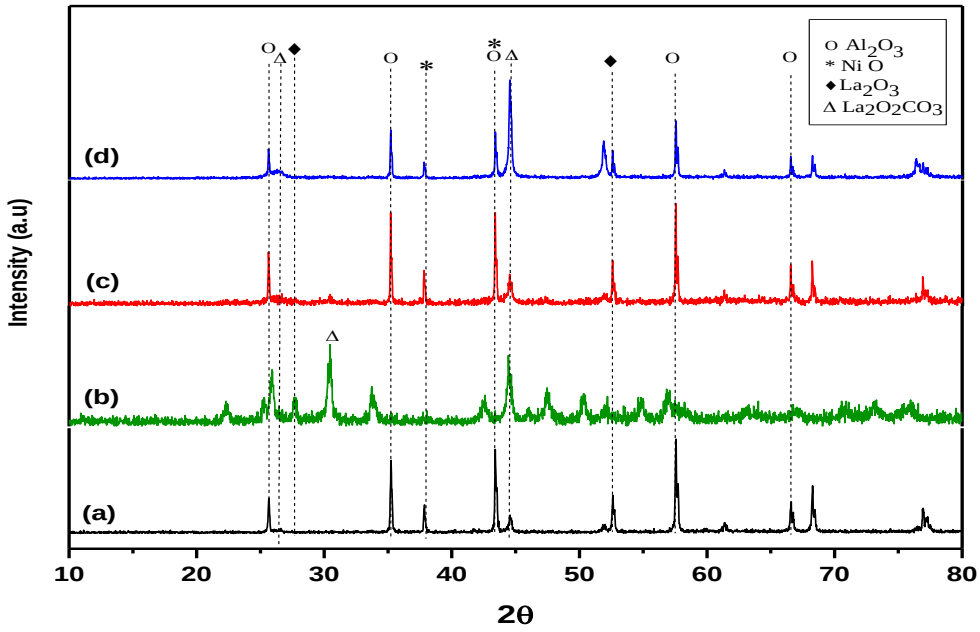


**Figure 6:** XRD of spent catalyst (a)5% $Ni/Al_2O_3$ (b) 5% $Ni/La_2O_3$ (c) 10% $Ni/La/Al_2O_3$ (d) 50% $Ni/La/Al_2O_3$

All spent catalyst was extracted via sieving and subjected to post-reaction characterization using XRD and PSD analysis. Figure 6 shows the diffractograms of all the spent catalysts. The diffractograms are almost the same as the synthesized catalyst, however, there are additional peaks that appear when Lanthanum is matching Lanthanum oxide carbonate ($La_2O_2CO_3$), PDF-File No 022-0642. The major peaks are at 25.9° (101), 30.4° (103) and 44.5° (110). However, no carbide

formation was observed [18]. This suggests that a new composite has formed as a derivative from the carbon coking and sintering hence deactivating the active sites on Nickel. This can also be reflected by the PSD analysis of the spent catalyst whereby the size comparatively increased approximately twice the synthesized catalyst size (Table 1).

## 5. 0 Conclusion

Ni-based supported nanocatalysts were successfully synthesized via the impregnation method. This was supported by the XRD analysis exhibiting pure phase crystal structure and PSD analysis showing all synthesized catalysts were within nano range. The addition of lanthanum proves that DRM can take place at a lower temperature. Moderate addition of lanthanum; 10%Ni/La/$Al_2O_3$ shows the best conversion and selectivity parallel to the DRM mechanism. This was more prominent at a higher temperature at 525 °C. The addition of lanthanum shows that it can reduce sintering by mesoporous framework confinement thus increasing selectivity. However, by increasing the lanthanum loading the conversion of methane increases rapidly to 72% favoring higher $H_2$ selectivity at 70 %. Catalyst deactivation still poses a major problem as the synthesized catalyst was deactivated from sintering as a result of coking when the temperature was raised to 550 °C. To conclude, by controlling the synthesis parameters such as active site selection, DRM reaction can occur at a lower temperature range.

## Acknowledgments

The authors would like to thank Universiti Malaya and Grant RU003-2021 for providing financial support in completing this work.

**Conflicts of Interest:** The authors declare no conflicts of interest.

## References

1. N. A. Rashidi and S. Yusup, An overview of activated carbons utilization for the post-combustion carbon dioxide capture. *J. CO2 Util*, **2016**. 13: p. 1-16.

2. S.-Y. Lee and S.-J. Park, A review on solid adsorbents for carbon dioxide capture. *J. Ind. Eng. Chem.*, **2015**. 23: p. 1-11.

3. E. Alper and O. Yuksel Orhan, CO2 utilization: Developments in conversion processes. *Petroleum*, **2017**. 3(1): p. 109-126.

4. D. Pakhare and J. Spivey, A review of dry (CO2) reforming of methane over noble metal catalysts. *Chemical Society Reviews*, **2014**. 43(22): p. 7813-7837.

5. N. El Hassan, M. N. Kaydouh, H. Geagea, H. El Zein, K. Jabbour, S. Casale, H. El Zakhem and P. Massiani, Low temperature dry reforming of methane on rhodium and cobalt based catalysts: Active phase stabilization by confinement in mesoporous SBA-15. *Applied Catalysis A: General*, **2016**. 520: p. 114-121.

6. A. Wolfbeisser, O. Sophiphun, J. Bernardi, J. Wittayakun, K. Föttinger and G. Rupprechter, Methane dry reforming over ceria-zirconia supported Ni catalysts. *Catal. Today*, **2016**. 277: p. 234-245.

7. Y. Wang, L. Yao, S. Wang, D. Mao and C. Hu, Low-temperature catalytic CO2 dry reforming of methane on Ni-based catalysts: A review. *Fuel Process. Technol.*, **2018**. 169: p. 199-206.

8. B. Abdullah, N. A. Abd Ghani and D.-V. N. Vo, Recent advances in dry reforming of methane over Ni-based catalysts. *Journal of Cleaner Production*, **2017**. 162: p. 170-185.

9. L. Zhang, X. Wang, C. Chen, X. Zou, W. Ding and X. Lu, Dry reforming of methane to syngas over lanthanum-modified mesoporous nickel aluminate/γ-alumina nanocomposites by one-pot synthesis. *International Journal of Hydrogen Energy*, **2017**. 42(16): p. 11333-11345.

10. D. D. Suppiah, Hamid, F. A., Kutty, M. G., Abd Hamid, S. B., Effects of titration parameters on the synthesis of molybdenum oxides based catalyst. *Sains Malaysiana*, **2012**. 41(10): p. 1245-1251.

11. D. D. Suppiah and M. R. Johan, Influence of solution pH on the formation of iron oxide nanoparticles. *Materials Research Express*, **2018**. 6(1): p. 015008.

12. E. Kok, J. Scott, N. Cant and D. Trimm, The impact of ruthenium, lanthanum and activation conditions on the methanation activity of alumina-supported cobalt catalysts. *Catal. Today*, **2011**. 164(1): p. 297-301.

13. M. Gong, W. Zhou, M.-C. Tsai, J. Zhou, M. Guan, M.-C. Lin, B. Zhang, Y. Hu, D.-Y. Wang, J. Yang, S. J. Pennycook, B.-J. Hwang and H. Dai, Nanoscale nickel oxide/nickel heterostructures for active hydrogen evolution electrocatalysis. *Nature Communications*, **2014**. 5: p. 4695.

14. E. Baktash, P. Littlewood, R. Schomäcker, A. Thomas and P. C. Stair, Alumina coated nickel nanoparticles as a highly active catalyst for dry reforming of methane. *Applied Catalysis B: Environmental*, **2015**. 179: p. 122-127.

15. P. Alphonse and B. Faure, Thermal stabilization of alumina modified by lanthanum. *Microporous Mesoporous Mater.*, **2014**. 196: p. 191-198.

16. N. Sun, X. Wen, F. Wang, W. Wei and Y. Sun, Effect of pore structure on Ni catalyst for CO2 reforming of CH4. *Energy Environ. Sci.*, **2010**. 3(3): p. 366-369.

17. A. J. Majewski, J. Wood and W. Bujalski, Nickel–silica core@shell catalyst for methane reforming. *International Journal of Hydrogen Energy*, **2013**. 38(34): p. 14531-14541.

18. L. J. France, X. Du, N. Almuqati, V. L. Kuznetsov, Y. Zhao, J. Zheng, T. Xiao, A. Bagabas, H. Almegren and P. P. Edwards, The effect of lanthanum addition on the catalytic activity of γ-alumina supported bimetallic Co-Mo carbides for dry methane reforming. *Applied Petrochemical Research*, **2014**. 4(1): p. 145-156.


Malaysian Catalysis
An International Journal